MASTER'S THESIS

Spatial modulation of light for ultracold gas experiments with erbium atoms

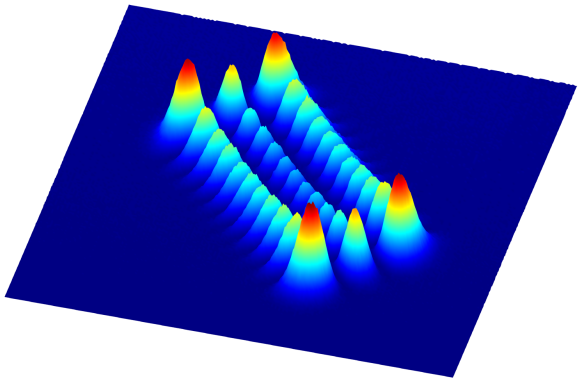

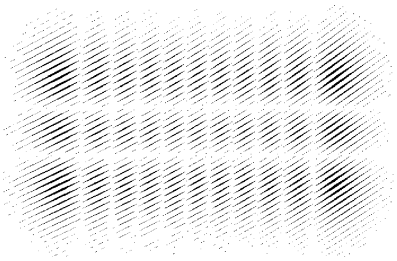

Daniel Petter

submitted to the Faculty of

Mathematics, Computer Science and Physics

of the University of Innsbruck

Supervisor:

Univ. Prof. Dr. Francesca Ferlaino

July 2015

Gewidmet meinen Eltern, meiner Schwester
und meiner Freundin, für ihre Liebe und Unterstützung.

Attention: This is not the original version of the thesis! Changes have been made to the original version to correct a number of spelling mistakes. The contents, however, has remained entirely untouched. The original version can be obtained directly from the author, or through the University of Innsbruck.

Abstract

In this thesis, we study a technique enabling the manipulation of the phase and intensity distribution of a laser beam by means of a digital micromirror device and possible implementations in ultracold quantum gas experiments. The scheme presented can be used to correct phase aberrations present in the system leading to diffraction-limited laser patterns. These patterns have broad applications. They can be used for example to address single atoms in an optical lattice, single ions or NV-centers in diamonds. Furthermore, the control over the laser beams intensity distribution allows a multitude of different beam profiles.

In a second part of the thesis, I will describe our work with ultracold, magnetic erbium atoms loaded into a three-dimensional optical lattice. Here I first introduce the extended Bose-Hubbard model, which includes magnetic dipole-dipole interaction. We study the superfluid to Mott insulator transition and observe for the first time nearest-neighbour interaction between the atoms, leading to an orientation-dependent energy gap in the spectrum of excitation in a Mott phase.

Contents

Introduction

Around 1924, when quantum theory was only a few decades old, an elegant derivation of Planck's formula, was described by Satyendranath Bose [Bos24]. His approach allowed Bose to deduce the frequency distribution of photons (which are bosons) of the radiation from a black-body. Picking up this approach, Albert Einstein derived the statistical behaviour of (massive) bosons, which is nowadays called *Bose-Einstein statistics* [Ein24]. In his work, Einstein showed first, that the statistics for bosons differs from the classical Maxwell statistics for ideal, classical particles. Secondly, he could predict a novel matter state for bosons, called *Bose-Einstein condensate* (BEC). This new state manifests itself in the appearance of a macroscopic occupation of a single quantum state.

It took around 70 years, from Einstein's theoretical predictions to the first experimental observations of BECs [And95, Dav95, Bra95]. One of the major technical developments towards the production of BECs, was the invention of the laser. It is a key ingredient, to cool and trap atoms. These first experiments were carried out with dilute clouds of alkali atoms, cooled down to temperatures on the order of hundreds of nanokelvin. At these temperatures the atoms accumulate in the lowest energy state of the used trap.

Up to date, 13 different atomic species could be Bose-Einstein condensed:

- alkali metals: Na [Dav95], Rb [And95], Li [Bra95], K [Mod01], Cs [Web02],
- alkaline-earth metals: Ca [Kra09] and Sr [Ste09]
- lathanides: Yb [Tak03], Dy [Lu11] and Er [Aik12]
- transition metals: Cr [Gri05]
- and H [Fri98], He [Rob01].

These different elements vary in their atomic properties. For example Cr, Dy and Er exhibit a large magnetic dipole moment, which gives an additional interaction between the atoms, known as the dipole-dipole interaction. The alkaline-earth species exhibit a non magnetic ground state and a narrow intercombination line, which makes them suitable for the implementation of highly precise clocks [Deg05, Blo14].

The technological knowledge for creating Bose-Einstein condensates was also used to cool fermions, which follow a different fundamental statistic. Identical fermions are not allowed, by Pauli exclusion-principle, to occupy the same state. Therefore fermions, cooled to ultracold temperatures simply fill up all quantum states in the system, from the lowest one up to a certain *Fermi energy*. Here the cloud of ultracold fermions is called a *degenerate Fermi gas* (DFG).

Over the last two decades, experiments with BECs and DFGs lead to a deeper understanding of the physical nature of these fundamental quantum systems. We have learned to control the interatomic scattering properties with *Feshbach resonances*, which allows to experimentally tune the interaction between the atoms from attractive to repulsive [Chi10]. These Feshbach resonances allowed to associate two atoms to weakly bound molecules like for example in Ref. [Joc03]. From there, they could be transferred with laser pulses into their ro-vibrational ground state [Ni08, Dei08, Tak14]. Some of them (heteronuclear molecules) can exhibit a large electric dipole moment, which opens up another strong and tunable interaction, additionally to the magnetic atoms. With Feshbach resonances also a tool to study the so-called *BEC-BCS crossover* became available [Bou04].

Bose-Einstein condensates and degenerate Fermi gases are also promising candidates for implementing quantum simulators, to simulate the behaviour of crystals. Here the atoms are loaded into optical lattices, which provide a periodic potential structure. First, main experimental results were obtained by observing the *superfluid to Mott* transition [Gre02] with bosons in a three-dimensional lattice. These systems can be used to investigate so called *Hubbard models* with bosons and fermions. Different species like heteronuclear molecules or the above mentioned magnetic elements Cr, Dy or Er can add additional interaction terms to these Hubbard models.

All these experiments rely on precise control of the used laser light. On the one hand, small defects in the lasers beam shape can lead to imperfections in the system and therefore to systematic errors. On the other hand, additional beam shapes would enable experiments to create even more complex systems.

The main goal of this master thesis was to develop knowledge for so called *spatial light modulation* techniques within our group. These techniques enable the control over the intensity and phase distribution of a laser beam. Therefore they can be used to shape laser beams in different manners, depending on the experiments needs. These methods have been used by several groups with ultracold atoms to achieve for example Bose-Einstein condensation in a uniform potential [Gau13], to address single atoms in an optical lattice [Fuk13] or for Bragg spectroscopy [Ha15].

In Chapter 1 I will give an introduction into spatial light modulation and explain two main devices, that are used for ultracold atom experiments, in more detail. These two devices are *liquid crystal spatial light modulators* (LC SLM) and *digital micromirror devices* (DMD).

Since we have decided to use a DMD, Chapter 2 will explain in more detail how a DMD can be used to create different potentials. After discussing the *imaging setup*, more emphasis is put on the *Fourier setup* in combination with a binary grating. The latter can be used not only to create different beam shapes, but also to correct phase aberrations present in the optical setup.

Chapter 3 will then present the experimental realisation of the Fourier setup with a DMD and will give results on what beam shapes could be created. The correction of phase aberrations is shown and also the limitations of the setup are discussed.

During the time of my thesis, I was also involved in the experiments of the ERBIUM group in Innsbruck. Therefore, Chapter 4 describes what we have achieved with erbium atoms loaded into a three-dimensional lattice. This system allowed us to investigate one of the above mentioned *Bose-Hubbard models* with an extension for magnetic, dipolar interactions. Here we could measure an additional term in the systems Hamiltonian, the so called *nearest neighbour interaction* for the very first time. In this chapter I will briefly summarise the apparatus and recent results of the experiment in Innsbruck. Then I will explain how optical lattices can be engineered and how our system can be described with the *extended Bose-Hubbard Hamiltonian*. Afterwards the measurement procedure and the final results are presented.

I conclude my thesis with an outlook on how our tested DMD setup could be used to perform *Bragg spectroscopy*.

Chapter 1

Basic concept of spatial light modulation

The term *spatial light modulation* summarises different techniques that enable control over the phase and intensity distribution of a light beam. This allows to 'shape' a laser beam according to the experimental needs. The importance of precise control of laser light, explains the use of spatial light modulation in various scientific fields. In astronomy it is used for example in adaptive optical systems to correct wavefront aberrations coming from the earth's atmosphere [Day02]. Spatial light modulation has also found its way into biology, where it is used for a lot of applications like retina imaging [Mu06, Abr10] or spatial light interference microscopy [Wan11], to name two examples. In physics spatial light modulation is used for example to shape femtosecond pulses [Wei00], to manipulate single atomic spins [Fuk13] or to prepare lines of atoms [Pre15] in optical lattices.

There are different techniques to achieve spatial light modulation. They vary mainly in their specific realisations, but the basic idea can be understood with Fig. 1.1. An incoming laser beam (sketched by green arrows) interacts with a so called *spatial light modulator* (SLM). Depending on which device one uses, the SLM can change the amplitude, the phase or both of the laser beam in a pixelated way. After the modulator an optical setup is needed, which defines a plane in which the shaped beam lies. This can be for example the Fourier plane of a single lense or the image plane of a microscope objective.

This thesis will focus on the application of spatial light modulation for ultracold atom experiments, where laser light is used to exert forces on the atoms. Here, the light is usually far detuned from any atomic resonance, which results in an approximately conservative potential - proportional to the intensity of the laser light, see Ref. [Gri00]. Therefore the created beam shapes can

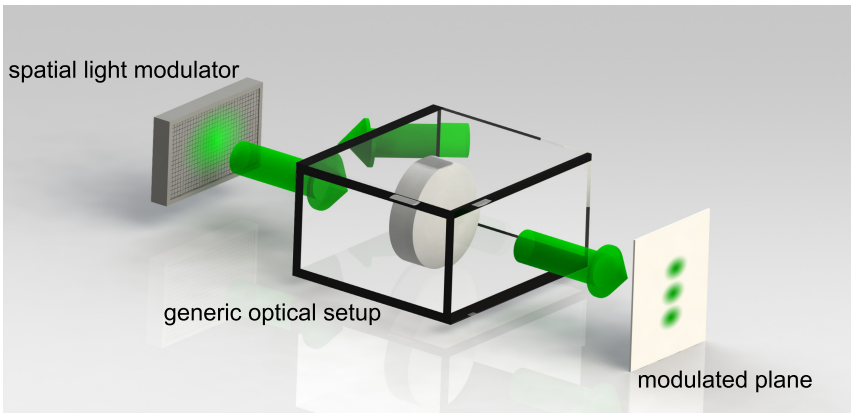

Figure 1.1: Main ingredients for spatial light modulation. A laser beam (green arrows), a spatial light modulator and an optical setup is needed to modulate the laser beam in a specific plane. For more information see text.

be used as a tunable light potential for atoms.

If we choose the Fourier plane of a single lens, the collimated laser light can be focussed down. This results in small patterns which allow high intensities in the created profiles. However due to Fourier limits, these beam shapes will be limited in edge sharpness (see for example [Zup13]). In contrast, the image plane allows bigger beam shapes with sharper edges, see Ref. [Bel11]. Additionally the imaging setup usually requires a good objective to scale the patterns down to typical sizes of ultracold atomic clouds, which range between a few micrometers in small traps up to tens of micrometers [Bil08, Mad00].

In this chapter I will discuss the two main SLMs, used to realise spatial light modulation. The liquid crystal spatial light modulator (LC SLM) and the digital micromirror device (DMD). However, for different applications there are also other tools on the market. Spatial light modulation can also be achieved with deformable mirrors [Dal05b] or piston mirror arrays. Since these two are not suitable for the realisation of this thesis, because of their low pixel number[1], they will be just mentioned here.

1.1 Liquid Crystal SLM

At the end of the 19$^{\text{th}}$ century Friedrich Reinitzer investigated *cholesterol* and observed an additional *'melting point'*, as he called it. When heating solid

[1] Currently the piston mirror array offers possible pixel numbers of only a few thousands. However, this might change in the future since they are still under development.

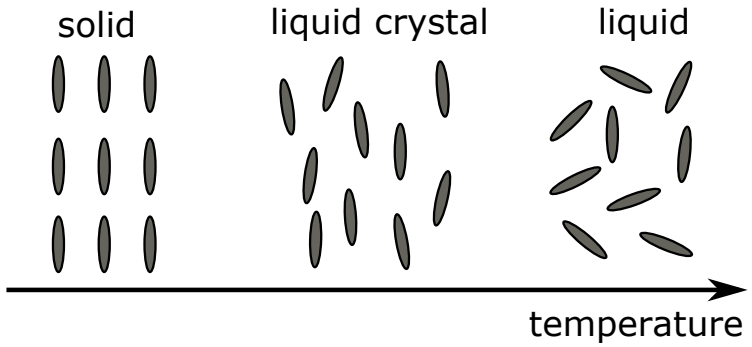

Figure 1.2: Different phases for liquid crystal materials. In the solid phase the molecules possess *positional* and *orientational order*, which are not present in the liquid phase. In between different liquid crystal phases can exist. The molecules do have a residual orientational order, but can for example move randomly. The phase illustrated here is called the *nematic phase*.

cholesterol up it turns into a diffuse liquid. When increasing its temperature even further it suddenly turns into a transparent liquid, see [Rei88]. This was one of the first observations of a *liquid crystal phase*, which some materials exhibit in between their solid and liquid state. I will now briefly introduce liquid crystals and discuss some of their basic properties, as it is at the basis of the LC SLM described here. For a more complete introduction, I refer to Ref. [Col90].

Liquid crystal phase

Usually materials with a liquid crystal phase consist of rod-shaped, complex molecules. In the solid phase, these molecules sit at a distinct place and have a certain orientation, they are called to have *positional* and *orientational order*. In contrast, the liquid phase has no order at all, here the molecules have a random position and orientation. In between, a state exists, where the molecules have lost its positional order from the solid phase but still have a residual orientational order. Thus the molecules can move randomly but have on average a certain direction in which they point together, see Fig. 1.2. This direction is usually called the *director*.

There exist a multitude of different liquid crystal phases. The phase shown in Fig. 1.2 is called *nematic phase*. There are two more prominent other phases. One is the *twisted nematic phase*, where the molecules do not align each other in parallel, but rather form a helical structure. The other is the *smectic phase*, where the molecules orientate each other in the same direction and organise

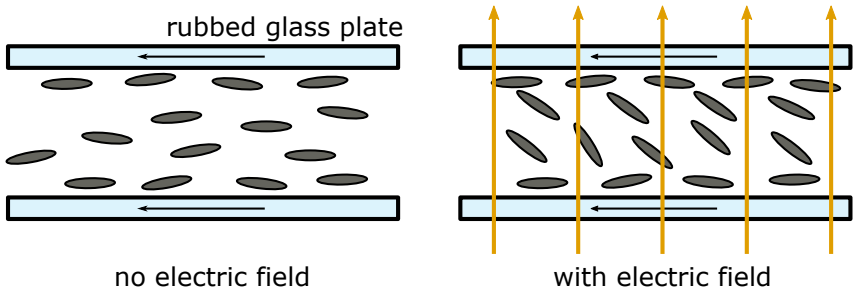

Figure 1.3: Left: When liquid crystals are placed between rubbed glass plates, the molecules align each other in the rubbing direction (small arrows). Right: An external electric field causes a rotation of the molecules in the more central region until a stable configuration is reached. The molecules at the glass plates do not rotate.

themselves in layers. Therefore a positional order in one dimension is here still preserved. Both types are thoroughly discussed in Ref. [Col90]. The twisted nematic phase is also widely used for spatial light modulators.

Liquid crystal molecules can either have a permanent electrical dipole moment or an induced dipole moment, when they are exposed to an electric field. In both cases, an external electric field rotates the molecules along the field lines. Therefore, the director of the liquid crystal phase will follow the electric field and can be tilted.

Light modulation with liquid crystals

For spatial light modulators, the liquid crystal is embedded between two glass plates. These glass plates are treated for example with chemicals, evaporated material or can be rubbed in a certain direction. This treatment gives rise to a preferred orientation of the liquid crystal as it ensures that the molecules close to the two plates have a fixed orientation, which they impart on the other molecules. In this way a preferred direction of the LC can be engineered, see Fig. 1.3 (left). When the molecules are now exposed to an electric field perpendicular to the glass plates, the molecules in the central region tilt in the direction of the field. During tilting, they pull their neighbouring molecules to adopt the same orientation. However, the molecules close to the glass plates do not rotate. This leads to a stable configuration of the LC which is depending on the electric field strength, see Fig. 1.3 (right).

One important property of liquid crystals is their birefringent character. Their director defines an optical axis, as in birefringent crystals. Depending

on the incoming lights polarisation the light beam will see certain indices of refraction corresponding to n_o for its ordinary ray and n_e for the extraordinary ray. The ordinary ray is polarised perpendicular to the plane, spanned by the optical axis (the director) and the travelling direction of the incoming laser light. The extraordinary ray is polarised in this plane and therefore has part of its polarisation along the optical axis. We assume now, that the incoming light is polarised along the orientation of the molecules shown in Fig. 1.3 (left), meaning that we put all the light into the extraordinary beam. When an electric field is applied, the direction of the optical axis of the liquid crystal changes. This changes the refractive index of the extraordinary beam $n_\mathrm{e}(V)$ with the voltage V used for the electric field. As has been pointed out in Ref. [Hu04] for this configuration one finds a retardation of the lights phase

$$\delta = \frac{2\pi d}{\lambda}\Big(n_\mathrm{e}(V) - n_\mathrm{o}\Big) \tag{1.1}$$

for the transmitted beam. It depends on the lights wavelength λ, on the distance d between the glass plates and on $n_\mathrm{e}(V)$. From this it can be seen, that by increasing the electric field, we can change the phase of the transmitted beam.

Liquid crystal SLMs can be operated in a transmitting or a reflecting configuration. The latter case is shown in Fig. 1.4. Here the incoming light enters from the top and gets reflected back on the mirror underneath the liquid crystal cell. The electric field is created with transparent electrodes on the upper glass plate and rectangular pixel electrodes under the mirror. These electrodes define single pixels of the liquid crystal SLM and they allow different electric fields in different pixels of the SLM. The molecules in these pixels will rotate more or less, depending on the electric field strength, leading to different phase retardations δ.

This constitutes one *phase-only* spatial light modulator. There are also phase-only modulators available with twisted-nematic phases, see for example [Kon88]. Besides phase-only modulators, there are also spatial light modulators that allow to change a beams intensity in a pixelated way. Here the reader is again referred to Ref. [Col90].

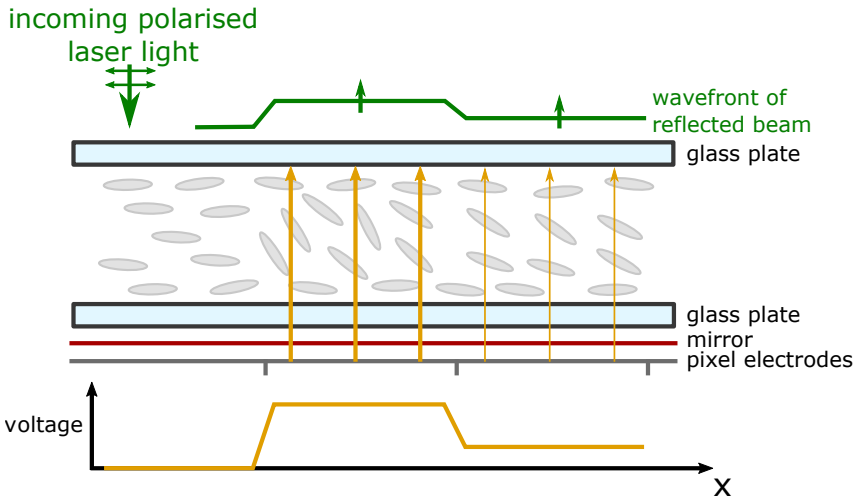

Figure 1.4: Schematic idea, how liquid crystals can be used to change the phase of an incoming laser beam in a pixelated way. The beam travels through the liquid crystal and reflects back at a mirror after wards. Individual electrodes underneath the mirror create electric fields across different regions of the LC. This allows a spatially resolved phase shift of the laser beam.

1.2 Digital Micromirror Device

Another spatial light modulator used nowadays is the digital micromirror device (DMD). The following section covers its basic properties and working principle. A complete description can be found in the manufacturers[2] manual in Ref. [TI13].

A DMD can be seen as a grid of about one million individual mirrors. Each mirror has an area of about 10x10 μm^2 and is mounted on a yoke that is attached to a torsion hinge, see Fig. 1.5. It can be tilted only to two angles, $+12°$ and -12°. These two angles correspond to an ON and OFF configuration. Therefore the DMD is said to have only *binary* pixels. Depending on which angle the mirror is tilted it can reflect light into one of two specific beam paths. The mirror position is set via two electrodes, that are situated underneath one diagonal of the mirror. Under each mirror there is a *dual CMOS memory* that defines the states of both electrodes complementary. First the memory is loaded with the state bits. One electrode is assigned with bit 1 and the other with the complementary bit $\bar{1}$. All mirrors and yokes share a common potential. This potential keeps in combination with the electrodes the mirror in its final position, see Ref. [Zup13]. Once a mirror is put into its position, it can stay

[2]Texas Instruments Inc.

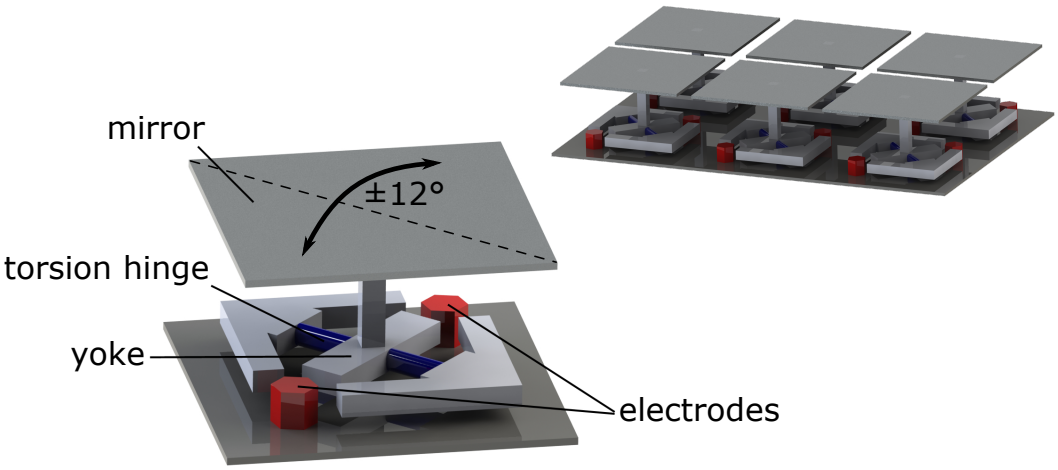

Figure 1.5: Schematic sketch of a DMD pixel. A mirror on a yoke is mounted on a torsion hinge that allows to tilt the mirror to two angles - $+12°$ and $-12°$. Electrodes underneath the diagonal of the mirror are used to define which position the mirror shall be tilted. Also plotted is a small array of the mirrors.

there until a new position is set. The maximum switching rate for the mirrors can be from 4 kHz up to 32 kHz, depending on the device.

All the mirrors are sitting on a *mirror board*. They usually span a rectangular area of about 1-2 cm^2, which is called *active area*. Besides this mirror board, an *interface board* is needed. This second board establishes the communication between the mirrors and a computer. It carries the necessary hard- and firmware and FPGA (field-programmable gate array) logic to control the behaviour of the whole device. It receives uploaded pictures from the computer, translates them into the necessary mirror states and sets the mirrors accordingly. The interface board contains usually an onboard RAM (random access memory), which allows to store pictures directly on the board. This is needed, if pictures shall be displayed with a frame rate, higher than the connection between the computer and the interface board allows.

Additionally a function library comes with the interface board. It allows to easily communicate with the board from the computer via a USB cable. Uploading, storing and displaying sequences can then be done easily by calling the appropriate function on the computer. The DMD used in this thesis is explained in more detail in Sec. 3.1.

1.3 Applications in ultracold atom experiments

Both devices, the LC SLM and the DMD, have been successfully used in ultracold atom experiments. In Ref. [Nog14] a phase-only LC SLM could be used to generate arrays of micro sized traps for rubidium atoms with nearest neighbour spacings down to a few µm. Here a phase pattern was imprinted on the laser beam with the SLM, leading to the desired trap geometries in the Fourier plane of a high numerical aperture (NA) lense.

Another experiment used a phase-only LC SLM to generate a quasi-uniform potential for Rubidium atoms [Gau13]. Here a blue detuned (repulsive) laser light was used to trap the atoms inside cylindrical-shaped potential walls. The precooled atoms could be Bose-Einstein condensed in this uniform potential.

The digital micromirror device was used to address single atoms in an optical lattice [Fuk13]. Here small patterns were created to induce light shifts on single lattice sites. These light shifts could then be used to resonantly drive spin flips of the corresponding atoms. The big advantage of the DMD here was that the atoms could sit in the image plane of a high NA objective. The image plane allowed to assign a small number of pixels directly to one lattice site. This allowed different lattice sites to be individually addressed at the same time.

One other experiment used the image plane of a DMD to perform *Bragg-spectroscopy*, see Ref. [Ha15]. Here a sinusoidal light pattern was moved over the atoms. From the speed of the moved pattern and its wave vector, the energy-momentum dispersion relation of a trapped atomic cloud could be mapped out. In addition the roton-maxon excitation spectrum of an ultracold atomic sample in a shaken optical lattice could also be measured with the same technique.

1.4 Comparison DMD and LC SLM

Some important properties of both devices are listed in Tab. 1.1 for comparison. For both SLM devices high resolution versions are available. Getting a concrete value for the diffraction efficiency[3] is difficult, since it depends strongly on the device and the used laser wavelength. Therefore the listed values should give just a rough estimate. Regarding the degrees of freedom (DoF) per pixel the LC SLM clearly outplays the DMD. Whereas the DMD only has binary pixels, the LC SLM typically offers more than 256 different voltage levels, which can be applied to one pixel.

[3] The amount of light that enters from the incoming beam into the modulated one.

The light utilisation[4] (LU) depends strongly on the created beam profile. In Ref. [Bel11] a phase only LC SLM with a Fourier setup yielded experimental LUs around 25 %. In the same thesis the DMD was used in an image configuration, where the LU for the same patterns was between 1 and 10 %, depending on the created pattern shape. In principle also patterns with a light utilisation of around 50 % are possible. As shown in this thesis, a DMD in a Fourier plane in combination with a binary, uploaded grating yields LUs with only around 1%. Here, the low light utilisation of the DMD is due to simply dumping beam power by turning mirrors OFF and is definitely the DMD's major disadvantage.

There is one important disadvantage of LC SLMs for ultracold atom experiments. If these liquid crystals are exposed to a constant electric field, the molecules undergo electro-chemical reactions over time and are destroyed. Therefore not a constant electric field, but rather an alternating one has to be used. This frame rate lies typically between a few Hz and 1 kHz, depending on the device. As has been shown in Ref. [Bel11], this results in intensity noise of the modulated beam, that has spectral peaks for frequencies of the switching rate and higher harmonics. Since trap and lattice frequencies in ultracold atom experiments lie typically in this regime, heating has to be expected coming from this switching rate. We have finally decided to use a DMD because here we do not expect intrinsic heating, due its static behaviour.

	Liquid Crystal SLM	**DMD**
resolution (pixels)	up to 1920x1080	up to 1920x1080
diffraction efficiency	60-95%	<86%
DoF per pixel	≥ 256	2 (ON/OFF)
intrinsic frame rate	between few Hz and 1 kHz	none
wavelength region	VIS, NIR	VIS, NIR

Table 1.1: Comparison of some main properties of a liquid crystal spatial light modulator and a digital micromirror device. Values for the diffraction efficiencies for the DMD are stated in different datasheets from Texas instruments but can in general be lower, since the mirrors diffraction efficiency depends also on the lights wavelength.

[4] What percentage of the diffracted light after the SLM is really used to achieve certain beam shapes.

Chapter 2

The digital micromirror device

The digital micromirror device (DMD) and its basic working principle is explained in Sec. 1.2. This section will show how it can be used for spatial light modulation. I will explain how the DMD can be seen as a blazed grating and how its main diffraction order can be found. Once the main order is known, it can be used for spatial light modulation. Afterwards the image setup and the Fourier setup is discussed. The latter one will be described in more detail, since it describes the basis of this work.

2.1 Blazed grating and phase aberrations

As mentioned in Sec. 1.2 the DMD consists of many tiny mirrors that are sitting next to each other. Therefore, the whole mirror area acts like a two dimensional blazed grating. This means, that the DMD itself inherently diffracts an incoming laser beam into different orders, see Fig. 2.1. For a given blaze grating geometry, one can calculate the main diffraction order m [Pal05], which carries most of the intensity[1], via

$$m\lambda = 2d\sin(\Theta_\mathrm{B}). \tag{2.1}$$

Here λ is the lasers wavelength, Θ_B is the tilt angle of the mirrors and d is the mirror spacing. For spatial light modulation, only this main order m is used. Once m is known, we can use the grating equation from Ref. [Pal05]

$$m\lambda = d(\sin(\Theta_\mathrm{in}) + \sin(\Theta_\mathrm{out})), \tag{2.2}$$

which connects the angle of the incoming laser beam Θ_in with the angle of the outgoing beam Θ_out for our main order m. We impose the that the main order

[1] The other orders carry in general less intensity and are not used for spatial light modulation.

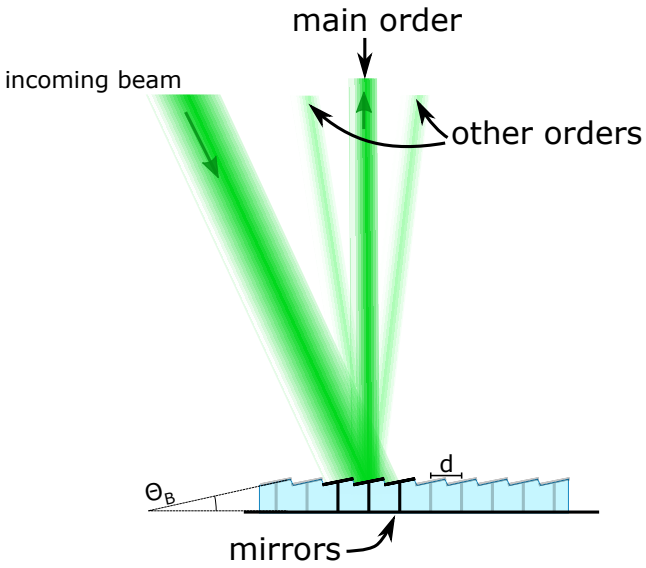

Figure 2.1: The mirrors of the DMD constitute a blazed grating. Therefore an incoming beam is diffracted in different orders. Depending on the mirror tilt angle Θ_B, the mirror spacing d and the wavelength of the laser light, a main order m will carry most of the intensity while the other orders will carry less.

beam travels perpendicular to the mirror area. Therefore we choose $\Theta_{out} = 0°$ and calculate the needed Θ_{in} under which we direct the beam on the DMD.

One important thing, which became visible during working on my master thesis, are phase aberrations induced by the DMD itself. These phase aberrations lead to a reduced beam quality after the DMD. According to Ref. [Zup13], these aberrations are coming mainly from the mirror area itself. The whole mirror array is pressed on a heating sink during manufacturing. This process bends the mirror area slightly, which distorts the wave fronts of the diffracted beam.

2.2 Image plane

One straightforward way to achieve modulation of the diffracted laser beam, is to image the plane of the DMD mirrors in an image plane. This is usually done with an objective, see Fig. 2.2. Here one pixel is imaged to a specific point in the image plane. For ultracold atom experiments, the created patterns are typically in the size of a few micrometer up to tens of micrometer. This has two important consequences. First of all, a good objective needs to be used,

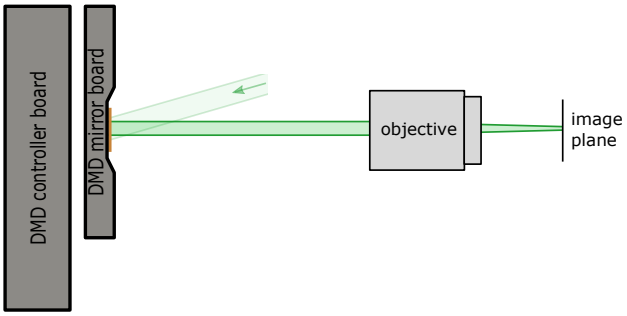

Figure 2.2: Image setup of the DMD. An objective is used to image the plane of the DMD pixels into an image plane, where for example ultracold atoms sit in an experiment.

to guarantee a high image quality at these small sizes. This limits the working distance of the objective, meaning the distance between the last lense and the image plane. Secondly, at this small sizes individual pixels can not be resolved by the objective and are washed out. Therefore multiple pixels contribute to specific areas in the image plane, which is good, because it allows for different intensity levels. For example, if 4x4 pixels contribute to one area in the image plane, than 16 different intensity levels can be applied by switching a certain number of pixels OFF.

A simple box-shaped potential can be generated like follows, see Ref. [Bel11]. First, a box of pixels on the DMD are turned simply ON and all the others OFF. This cuts out a square-profile out of the Gaussian incoming beam. However, the truncated beam still has a Gaussian envelope on top of the box shape. This can be corrected, by turning certain mirrors OFF in the more central region, to reduce the intensity coming from this region. This technique uses the so called *error diffusion algorithm*, which allows to calculate which specific mirrors need to be turned OFF to achieve a certain intensity profile in the end. With this setup, one can directly 'cut' out a multitude of beam shapes like rings, walls, lines and so on.

2.3 Fourier setup

Another approach to achieve spatial light modulation is to take a Fourier setup. Here a single lense can define a Fourier plane, see Fig. 2.3. The connection between the diffracted beam at the mirror plane and the Fourier plane is now given by the Fourier transformation. Compared to an imaging setup, no objective is needed and, since all the light of the beam is focussed down, higher

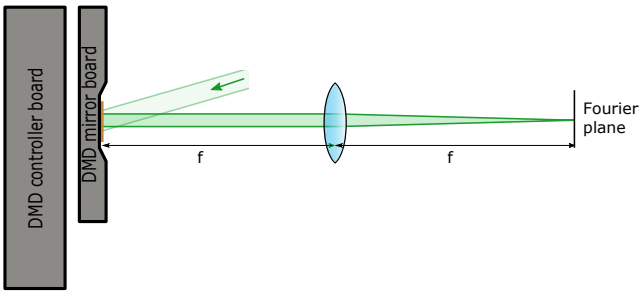

Figure 2.3: Fourier setup for spatial light modulation. The diffracted beam is focussed in the Fourier plane of a single lense.

intensities can be reached. However, these advantages come at the cost of edge sharpness of the beam shapes, because the patterns will be Fourier limited. Here, for an infinitely sharp potential, like a box, an infinite number of Fourier components would be needed. However, these can not be provided due to the finite size of the DMD mirror area.

Compared to the imaging setup, there exist techniques that allow to correct phase aberrations in the Fourier plane. In this section I will introduce the idea of a programmable grating, that can be uploaded on the DMD and used for correcting phase aberrations in the setup and also for displaying different intensity patterns. The main ideas come from another master's thesis, Ref. [Zup13], where the whole technique has been demonstrated with great success.

Capabilities of a displayed grating

Since the DMD allows us to program the state of each individual mirror independently, we can upload any imaginable pattern within the resolution of the device. This also means, that we can upload a binary grating pattern on the DMD, by tilting stripes of mirrors ON and other stripes of mirrors OFF. The width of one of these stripes is given by the amount of neighbouring mirrors that are turned to an ON state. We can change the width of these stripes in certain regions of the grating, as we want. Additionally, these stripes do not have to be straight lines, but can be bended.

To see how powerful these properties of a programmable grating are, we have a closer look at it on Fig. 2.4. Here a (one dimensional) grating is represented by black slits. It reflects an incoming laser beam into different orders,

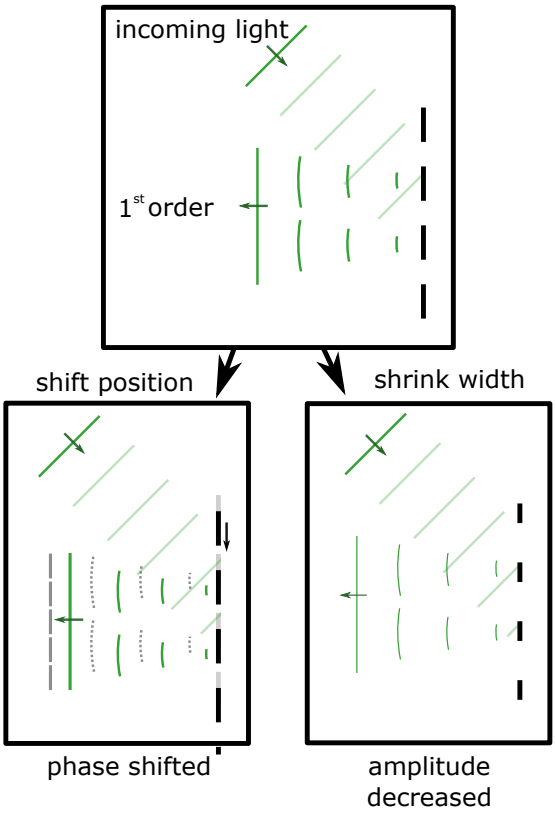

Figure 2.4: The first order of a grating can be used for spatial light modulation. The grating allows us to change the beams phase, via shifting the grating, and lower its amplitude via shrinking the width of its stripes. The combination of both enables us to create arbitrary wavefronts of the first order.

from whose only the first order is important for now[2]. As explained above, the programmable grating allows us to change both, the width and the position of our stripes locally on the DMD. On the one hand, a shift of the stripes positions will shift the phase of the diffracted beam (one simple picture is that the incoming wavefront sees the grating at a different time). On the other hand, a decreased stripe width will attenuated the beams intensity. This results in a complete control over the first order beams phase and amplitude even though

[2]It is important to notice that this uploaded grating gives us diffraction orders $0, \pm 1, \ldots$ *on top* of the used m order of the blazed grating, that the DMD constitutes. So also the weaker other orders of the blazed grating show these diffraction orders of the uploaded grating on top of them, but with much less intensity.

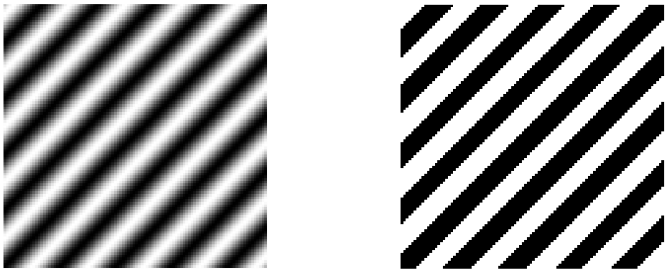

Figure 2.5: Binarisation of a grating function. The DMD can take only the two values 0 (white) for OFF and 1 (black) for ON for the mirror states. Therefore the values for a sinusoidal grating (left) need to be mapped into the either 0 or 1. The most straight forward way is to round the grating value. One pixel on the binarised grating (right) corresponds to one mirror state. This example is for a square of 100x100 mirrors.

our DMD itself can only affect the amplitude of the incoming beam.

Keeping these two properties in mind, we will see in this Chapter how we can correct phase aberrations in our system and how we can change the intensity distribution in our final, phase-corrected beam shape. Especially a good correction for phase aberrations will be necessary for diffraction-limited performance of our light modulation setup.

We first need to find a formula $f_{\text{grating}}(x, y)$ which allows us to create a grating pattern, that we can upload on the DMD. This formula is then applied to a two dimensional matrix, in which each entry corresponds to the state of one mirror, such that one mirror represents one pixel in the grating pattern. After uploading this final matrix on the DMD, the grating pattern is displayed and shall result in the needed beam profile in the Fourier plane. Since the DMD can interpret only two integer values (0 as OFF and 1 as ON), one straight forward way to initialise the mirror states is to round each pixel value generated by f_{grating}. This gives us a binary grating pattern where each matrix element has either 0 or 1, see Fig. 2.5.

One possibility to represent a grating is to use

$$f_{\text{grating}}(x, y) = \frac{1}{2}\left(\sin\left(\vec{k} \cdot (\vec{x} + \vec{y}) + \phi(x, y)\right) + 1\right). \tag{2.3}$$

Here f_{grating} defines a two dimensional sinusoidal pattern that has a wave vector in direction $\vec{k}$ and has values between 0 and 1. Additionally, a phase $\phi(x, y)$ can be added, which will allow us to modify our grating. For example if

$$\phi(x, y) = \text{constant}$$

the original grating is simply shifted, which simply shifts the whole phase of our first order beam. It is straightforward from Eq. (2.3), that a linear phase gradient

$$\phi(x, y) = \vec{k'}(\vec{x} + \vec{y})$$

results simply in another linear grating with a new wave vector $\vec{k}_{\text{new}} = \vec{k} + \vec{k'}$. Note that this different wave vector results in a different refraction angle of the first order beam and therefore will shift its position in the Fourier plane.

If one considers more complex phases $\phi(x, y)$ one can imagine, that the original grating gets more and more distorted, but also that certain parts of our first order beam can have different phases and positions in the Fourier plane.

In an ideal optical setup, the first order beam of our programmable grating would be again a Gaussian beam (assuming the incoming beam is Gaussian). However, the lense used for the Fourier plane and the DMD itself introduce aberrations, which lead to a distorted beam in the Fourier plane. Therefore it is necessary to measure these phase aberrations and correct for them with the grating, in order to get an ideal Gaussian beam shape back. We will see in the following section, how these aberrations can be measured. Once we have a map for our phase aberrations, we can directly apply the conjugated phase map $\phi(x, y)$ to the grating in Eq. (2.3).

In the following two sections I will introduce the concept of the *phase map*, which directly contains all necessary information to correct aberrations, the *intensity map* and the *profile map*, which in the end gives us the intensity distribution of our shaped beam profile.

The phase map

As discussed before, by introducing a phase map $\phi(x, y)$ for our grating, we can control the phase and the position of different parts of our first order beam in the Fourier plane.

The first goal is to measure the phase aberrations present in the whole optical system to be able to correct them. To measure the (relative) phase aberrations in different regions of our setup, we need to define a reference phase. This can be done by displaying a small rectangular part of our grating, which we call *reference patch*. This reference patch results in a small beam with a certain phase in the Fourier plane, where we can put a camera. When displaying a second *sampling patch*, the corresponding beam will interfere with the beam associated with the reference patch, see Fig. 2.6. From the resulting interference pattern we can retrieve the relative phase difference between the sampling and the reference patch, as we will see now. The two beams can be

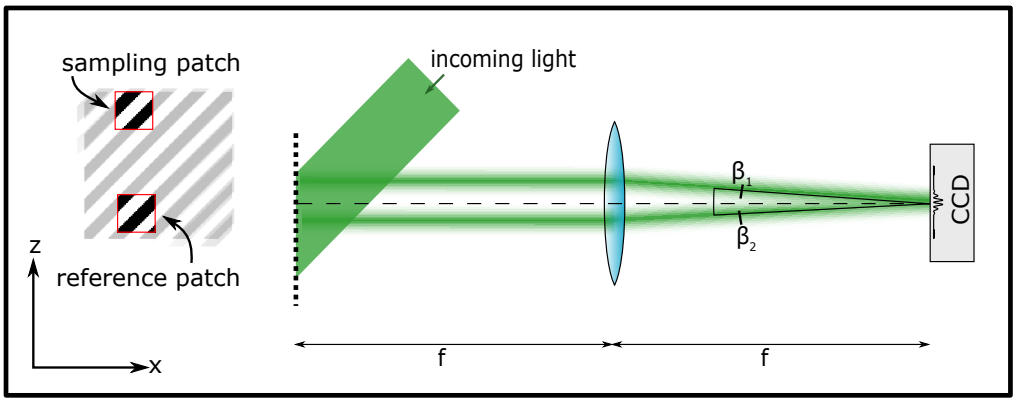

Figure 2.6: To measure the relative phase aberrations, one needs to display two small patches of our grating. One reference patch and a sampling patch. Both patches will create two beams that will interfere in the Fourier plane. From the interference pattern, we can extract the phase aberration between these two patches.

described by plane waves that are travelling under certain angles[3] β_1 and β_2 to the optical axis x

$$E_1 = A\mathrm{e}^{\mathrm{i}k(\sin(\beta_1)z+\cos(\beta_1)x+\Delta\phi)} \tag{2.4}$$

$$E_2 = B\mathrm{e}^{\mathrm{i}k(\sin(\beta_2)z+\cos(\beta_2)x)}. \tag{2.5}$$

Here, z is the axis between the two patches, $k = 2\pi/\lambda$ is the lasers wavenumber and A and B the amplitudes of the electric fields. Additionally a phase $\Delta\phi$ for the sampling beam is used, which considers the phase aberration from the setup. Looking at the interference pattern in the Fourier plane at $x = f$, we get

$$|E_1 + E_2|^2 = A^2 + B^2 + 2AB\cos\Big[k\Big(z\sin(\beta_2) - f\cos(\beta_2) - \\ - z\sin(\beta_1) + f\cos(\beta_1)\Big) + \Delta\phi\Big] \tag{2.6}$$

with f being the focal length of the lense. We see that we get an interference pattern with a wave vector, which depends on the angle of our beams, and with a shifted phase $\Delta\phi$ that comes from aberrations. In Ref. [Zup13], the interference pattern was moved over a photodiode with a small pinhole in front. In our experimental setup in Chapter 3 we will use a CCD camera, which gives us directly a full picture of the interference pattern, which we then can fit with

[3] For simplicity we neglect the lights polarisation here.

Eq. (2.6). From this fit, we can extract $\Delta\phi$. It is now straightforward to scan the position of our sampling patch to get the phase aberrations $\Delta\phi$ for a region around our reference patch.

Typically, the pixel size of the CCD camera is in the order of a few micrometers (or bigger) and hence does not allow to measure the phase aberrations with the same reference patch for all scanned patches. The reason is, that for bigger distances between reference and sampling patch, the wave vector of the interference pattern gets bigger. For bigger distances between the two patches, the angles β_1 and β_2 in Eq. (2.6) get bigger and the distances in the interference pattern become smaller. Therefore, at a certain distance between the two patches our camera will not be able to resolve the interference pattern any more. Therefore, no fit can be applied and no phase aberration extracted. We have defined an approach that circumvents this issue and aims to retrieve a complete phase map for the whole mirror area of the DMD. The idea is to scan the DMD area with smaller phase maps, which we can resolve with our camera.

First, we have a look at two different small phase maps. They use different reference patches, which differ in phase and in position. The difference in phase comes from the fact that the two beams corresponding to the reference patches have travelled a different way. The difference in position arises from the fact that each reference beam is not focussed to the same spot. Now, each small phase map gives a phase correction with respect to their reference patch. However, since the reference patches differ, the small phase maps correct light from the associated sampling region of the DMD differently. Therefore we need to find a way to match the two small phase maps by matching their two reference patches. Considering Eq. (2.3) we can add to one of the two small phase maps another phase map

$$\phi_{\text{match}}(x, y) = \text{constant} + \vec{k'}(\vec{x} + \vec{y}) \tag{2.7}$$

that has a constant and a linear contribution. it is possible to choose this contribution such that the position and the phase of our two reference beams coincide, which directly matches the two small phase maps.

To compute $\phi_{\text{match}}(x, y)$ one possibility is to measure two small phase maps that overlap. Taking the difference will directly give us the constant offset and the linear gradient that we need. It can be added to one of the two small phase maps and results in a matched bigger phase map. Then, this scheme can be applied to a next small phase map, and so on, until the full phase map is recovered from multiple small phase maps. How good this method works and what its limits are, will be exposed in Chapter 3.

The intensity and profile map

Once we have a phase map, that corrects for phase aberrations, we are back on the ideal configuration, where the first order beam has a Gaussian shape. If we want to create different beam profiles, we have to cut our pattern out of this Gaussian beam. This is done by locally decreasing the stripe widths of our grating and therefore the intensity coming from different regions of the DMD.

The intensity distribution on the Fourier plane depends on the intensity distribution on the DMD mirrors. For that reason, we first need to measure the intensity distribution of our incoming laser beam. This can be done by displaying a single grating patch on the DMD and integrate the intensity of the first order on the camera. By scanning again the position of this patch, we get an intensity map $A_{\text{int}}(x, y)$ whose resolution is set by our patch size. Since we expect our incoming beam to be smooth and Gaussian, a bigger patch size than for the phase map can be used. This map can be normalised and is proportional the intensity distribution of our incoming beam. It is used to take the different incoming intensities on each DMD mirror into account.

In a next step we create a normalised profile map $A_{\text{profile}}(x, y)$, which contains the Fourier transform of the pattern we want to create. This can be for example a TEM_{03} mode or even a discrete Fourier transformation of our final pattern. We can define a new locally weighted map

$$A_{\text{local}}(x, y) = \frac{A_{\text{profile}}(x, y)}{A_{\text{int}}(x, y)} \tag{2.8}$$

which is a profile map whose values are weighted by the inverse of the incoming intensity distribution. This means that points with less incoming intensity get increased compared to points with higher incoming intensity. The reason for this can be understood, if one looks at a (one dimensional) box-like profile map with a Gaussian incoming beam, see Fig. 2.7. If we would simply display a box profile, the beam after the mirrors would still show a Gaussian envelope on top, due to the Gaussian incoming intensity. Therefore the amplitude of the profile map has to be decreased in the center region to recover a flat intensity[4] directly after the DMD.

The final locally weighted map $A_{\text{local}}(x, y)$ is used to assign stripe widths to our grating. After normalising $A_{\text{local}}(x, y)$, each point defines us a cutoff for our grating in Eq. (2.3). Its value can be calculated from a one dimensional cosine wave to

$$c_{\text{cut}}(x, y) = \frac{1}{2}\Big(\cos\big(\operatorname{asin}(A_{\text{local}}(x, y))\big) + 1\Big). \tag{2.9}$$

[4]Notice here, that a box shaped profile pattern on the DMD would yield in the Fourier plane a two dimensional sinc-shaped pattern.

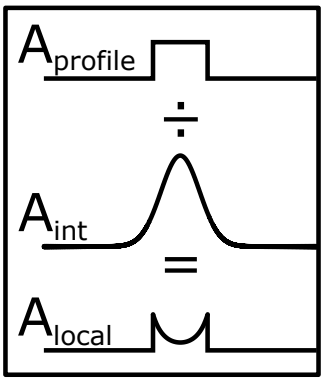

Figure 2.7: Schematic idea of the locally weighted map A_{local}. The profile map A_{profile} is defined by the Fourier transform of the final pattern. In order to compensate for an inhomogeneous incoming intensity distribution, an intensity map A_{int} needs to be measured whose inverse acts as a weight for the profile map. For more information see text.

If the value of our grating $f_{\text{grating}}(x, y)$ is now bigger than $c_{\text{cut}}(x, y)$ the corresponding pixel is turned ON. If the value is lower, the mirror is turned OFF.

Chapter 3

Experimental realisation

Once we have decided for the DMD, we could choose between an imaging setup, where usually a high NA objective is used, or a Fourier setup. Both approaches have been implemented with great success in optical lattice experiments with single-site resolution [Fuk13, Pre15]. The current Erbium experiment in Innsbruck has no possibility for optical access with high numerical apertures, since the viewports of the main chamber limit us to NA≈0.1. Therefore it can be hard to get qualitatively good and small light patterns at the point of the atoms. One would have to think about an optical setup that demagnifies the beam coming from the DMD by a factor of 50 to 100 to get shapes in the size of 100 µm. Additionally the distance between the last lense and the image plane should be around 10 cm working distance. The impossibility of correcting phase aberrations in an image setup yields even more carefully designed optics. On the other hand the Fourier plane seemed more appropriate for our purposes, since one single lense can already give a Fourier plane that can lie at a far enough distance after the lense to be implementable in the experiment.

This Chapter discusses the experimental realisation of light modulation with a Fourier plane. I will first describe the characteristics of the DMD and our optical setup. I will then describe how the phase map and the intensity map can realised. Using these two maps, we can directly start creating patterns, which will then be analysed in more detail. Finally, the possibilities, the limitations and future improvements of this Fourier approach for the DMD are discussed.

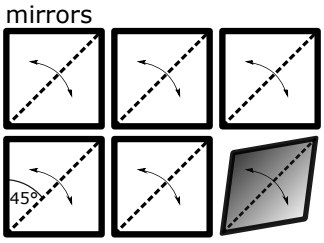

Figure 3.1: Tilting of the mirrors about its diagonal axis. To keep the reflected beams in the same horizontal plane, the DMD has to be mounted at 45°.

3.1 Technical characteristics of the DMD and the optical setup

Our DMD[1] consists of two boards: The *mirror board*[2] on which 1080x1920 aluminium mirrors are mounted and the *controller board*[3], which is the interface between the computer and the mirror board. The latter can be directly attached via USB to a computer. The two boards are connected via two flexible cables.

Each square mirror has an area of 10.8x10.8µm^2 and can be tilted to two stable angles +12° and -12° (corresponding to ON resp. OFF state). The mirrors have a maximum switching rate of 17.8 kHz. Additionally the controller board has an onboard RAM (random access memory) which allows the storage of 31.000 binary patterns. This allows us to upload sequences of patterns directly on the DMD and display them with high pattern rates.

When installing the DMD we need a mount for the mirror board and a casing for the controller board. Especially for the mirror board one has to consider a few factors. First of all, the mirror board should be mounted as stable as possible to avoid temporal and spatial noise of the final pattern. Secondly, when a mirror is switched, it tilts about its diagonal axis, see Fig. 3.1. A rotational axis, at an angle of 45° from the vertical, would reflect the incoming laser beam out of the horizontal plane of the optical table. Therefore the whole DMD needs to be tilted by these 45°, to have the rotational axis of the mirrors pointing vertically. This allows to flip the mirrors along the vertical axis and keeps all reflected beams in the same horizontal plane. To fulfil these requirements, I have designed a mounting for the mirror board. It was machined in the universities mechanical workshop.

[1] Discovery 4100 Development Kit from Vialux
[2] DMD 0.95 inch 1080p VIS from Vialux
[3] DLP Discovery 4100 Main Board from Vialux

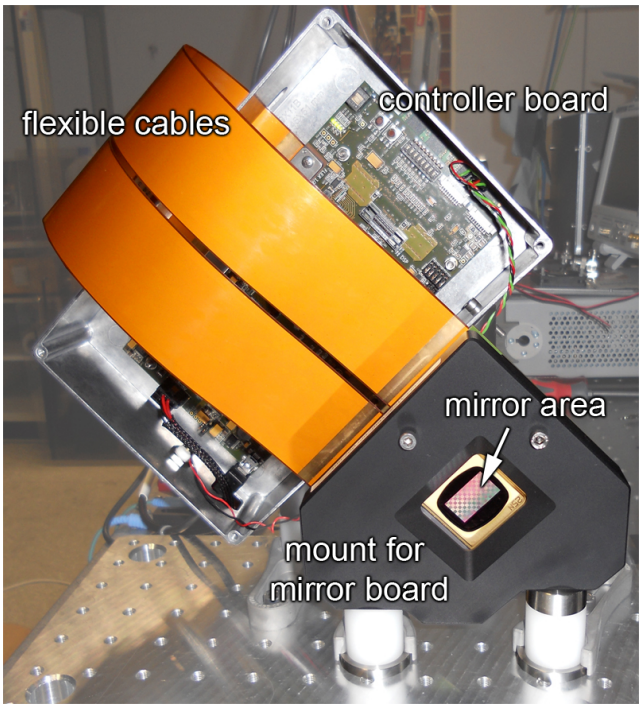

Figure 3.2: Casing for the DMD. The mirror board (front) is mounted on a self designed holder. For the controller board (back) a normal aluminium box is used. It is also mounted at 45° angle to avoid shearing forces on the flexible cables.

The casing for the controller board is not as critical as the mount for the mirror board. Here I simply modified an aluminium box which is air cooled by two fans. To avoid shearing forces on the flexible cables, the controller board is also mounted at 45°. The whole DMD is shown in Fig. 3.2.

As illustrated in Fig. 3.3, we test the DMD with a simple optical setup. We use a few milliwatts of 532 nm laser light from a diode-pumped, frequency doubled laser[4]. The light is delivered from the main optical table via a fiber. After the fiber, a polarising beam splitter (PBS) cube is used to clean the light polarisation. The light is then sent through an acusto optical modulator[5] (AOM) with a driving signal frequency of 110 MHz. The AOM splits the light into different orders $0, \pm 1, \ldots$, that are travelling in slightly different directions. All orders, except the $+1$ order, are blocked with an iris. The intensity of

[4] Verdi$^{\mathbf{TM}}$ V-10 single frequency, diode-pumped laser with 10 Watt max. output from Coherent.

[5] AOMO 3110-120 from Gooch & Housego

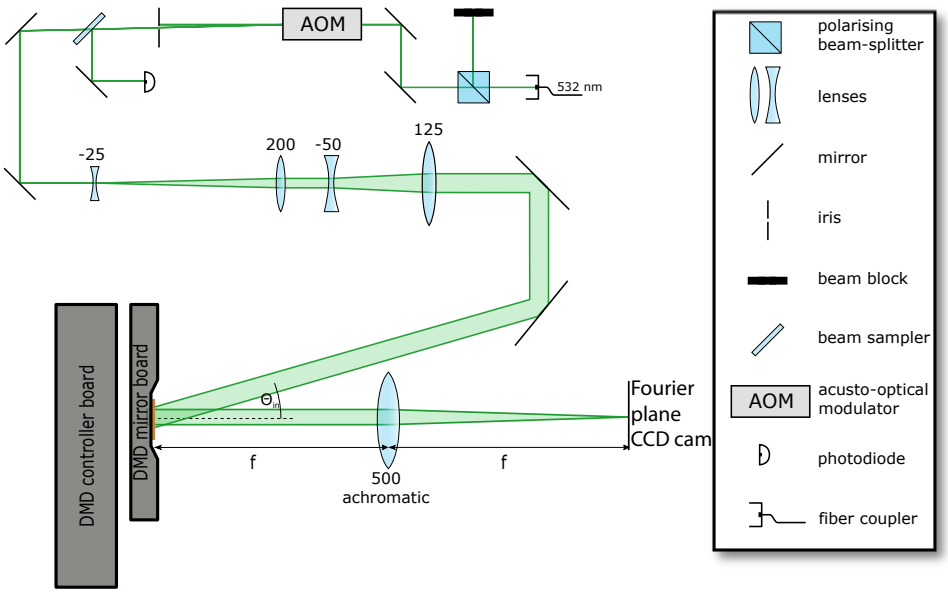

Figure 3.3: Setup for beam preparation. The laser light comes from a fiber and is first polarisation cleaned via a PBS cube. The first order of an AOM in combination with a photodiode and a PID controller allows to stabilise the intensity of the laser beam. Afterwards a double telescope expands the beam to a waist of roughly 1 cm. For further details see text.

the +1 order depends on the amplitude of the AOMs driving signal. A beam sampler after the iris reflects a small portion of the beam on a photodiode. The photodiode signal can now be stabilised with a proportional-integral-derivative controller (PID). The PID has two inputs and one output part. One input is for the photodiode signal, the other is used as a *set value*, which can be externally varied. The output port is connected to the amplitude of the driving signal for the AOM. The PID now keeps the photodiode signal at the set value, by changing the driving amplitude. This stabilises the +1 order of the AOM, which is then used for the DMD.

After the beam sampler, we expand the beam to a waist of roughly 1 cm, to cover all the mirrors of the DMD. This is done via two telescopes that are shown in Fig. 3.3.

As explained in Sec. 2.1, the DMD acts like a two dimensional blazed grating. Therefore, it diffracts an incoming laser beam into different diffraction orders, from which one order m carries most of the intensity. From Eq. (2.1),

we calculate the main diffraction order of the DMD to

$$m \approx 6.$$

From Eq. (2.2) and considering $\Theta_{\text{out}} = 0°$ we obtain an incoming angle of

$$\Theta_{\text{in}} \approx 17.5°.$$

The expanded laser beam is then directed on the DMD under Θ_{in} (measured from the axis perpendicular to the mirror area), see Fig. 3.3.

After the DMD we use an achromatic, two-inch lense with a focal length of $f = 500\,\text{mm}$. Its numerical aperture is $\text{NA} = \sin(\alpha) \approx 0.05$ where α is the half angle of the maximum light cone. For a wavelength of $\lambda = 532\,\text{nm}$ we get a resolving power, according to Ref. [Joh60], of $\text{R} = \frac{1.22\lambda}{2\text{NA}} \approx 3.2\,\mu\text{m}$.

In the Fourier plane of the lense we put a CCD camera[6] with 1360x1024 pixels and a pixel size of $4.65\text{x}4.65\,\mu\text{m}^2$. With this camera we will now measure the phase aberrations, the amplitude map, and check the created beam patterns.

3.2 Phase and amplitude map

After setting up the optical setup, we first put *all* mirrors to an ON state. On the CCD camera we see the bright $m = 6$ order of the blazed grating appearing[7].

Phase map

We follow the approach discussed in Sec. 2.3. A grating pattern is uploaded on the controller board of the DMD and the mirrors are set accordingly. On the camera, the main $m = 6$ diffraction order shows now three diffraction orders of the uploaded grating. One is the main order which carries most of the intensity and the other two are first orders, see Fig. 3.4. Higher orders are not visible[8] on the camera. One of these two first orders can be used to implement spatial light modulation as described in Sec. 2.3. We therefore restrict our camera area to one of this first orders.

[6] mvBlueFox-233G from Matrix Vision

[7] Compared to the $m = 6$ order, the other orders of the blazed grating are only visible on the CCD camera for longer exposure times.

[8] Note again, that these main and first orders are coming from the same $m = 6$ order of the diffracted beam from the blazed grating.

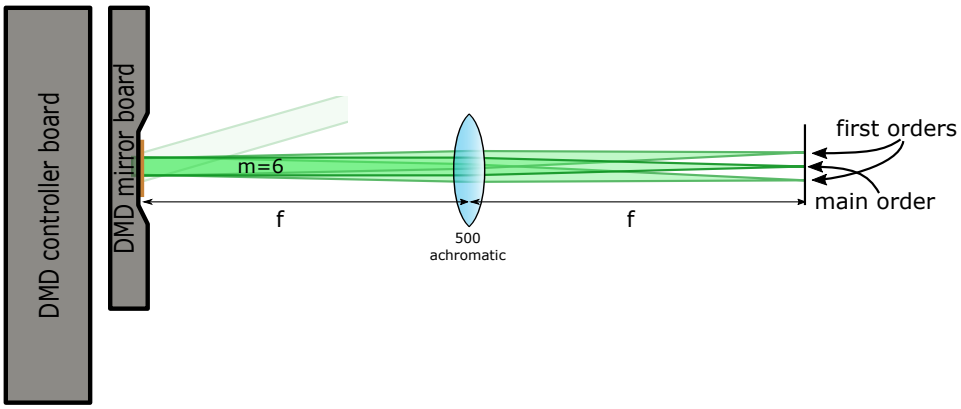

Figure 3.4: After uploading a grating pattern on the DMD, the $m = 6$ order beam of the blazed grating splits in three orders, one main order and two first orders. For spatial light modulation, only one of the two first order beams are used.

At the beginning, the phase aberrations need to be measured. First, only a reference patch of 20x20 mirrors is displayed on the DMD, which gives a Gaussian spot on the camera. From this we extract the center position of the pattern via a Gaussian fit. This center position is taken as a reference point for phase aberration ϕ, which is measured in a next step. Secondly, a 20x20 mirrors sampling patch is displayed in addition. The reference patch is now kept at a fixed position, while the sampling patch is scanned over an area of 15x15 patches, see Fig. 3.5 (left). Each position of the sampling patch results, in combination with the reference patch, in an interference pattern on the camera, see Fig. 3.5 (right).

Each of these interference patterns are fitted with a plane wave and a Gaussian envelope[9]. The center of the Gaussian envelope is fixed by the center position of the precursory Gaussian fit, where only the reference patch was displayed on the DMD.

For each interference pattern we get a phase value $\Delta\phi$ from its fit, which can be assigned to the corresponding sampling patch. What we get is a small phase map corresponding to the 15x15 area of sampling patches, see Fig. 3.6 a). Since our fits of the interference patterns can only extract phase aberrations *modulo* 2π, this small phase map first needs to be unwrapped. This is done

[9]We have also implemented a fit of a plane wave without Gaussian envelope, around the central region of the interference pattern. The resulting phase ϕ is the same, but the time for calculating decreased dramatically, because less pixels need to be fitted.

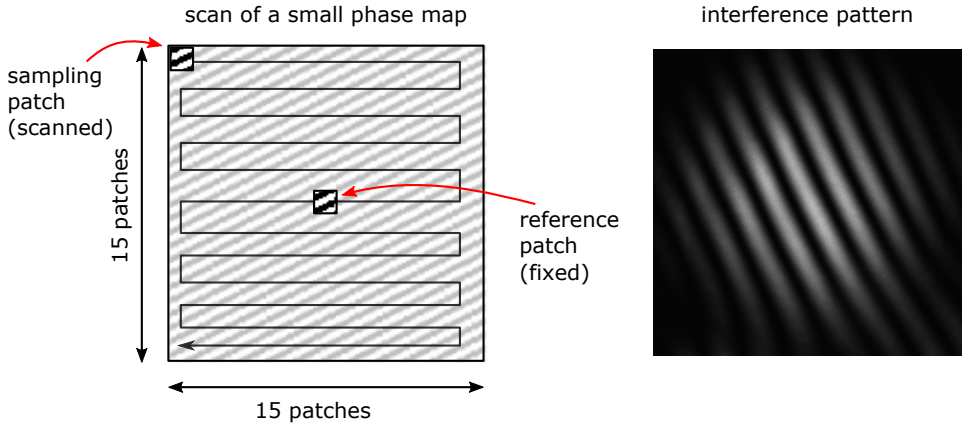

Figure 3.5: Left: Scan of a small are of 15x15 patches on the DMD. The phase aberrations are measured between a reference patch and a sampling patch. The grey background illustrates the used grating, which is not displayed. Right: Interference pattern between reference patch and a sampling patch in the Fourier plane, taken with the camera. From this interference pattern the phase aberration is extracted with a fit.

with an *unwrapping algorithm*[10] which corrects for 2π jumps. The unwrapped small phase map is illustrated in Fig. 3.6 b). For some maps the unwrapping did not work for border pixels. Therefore we decided to always cut away one line of pixels at the border, to fully automate the calculation procedure. There are still some bad points inside the small phase map, which are coming from a failed fitting of some interference patterns. These points can be eliminated, by fitting the whole small phase map with a two dimensional locally weighted regression[11]. In the end, a smooth phase map for our sampling area is obtained, see Fig. 3.6 c). This would already allow a phase correction for this specific area of the DMD.

Since we want to use as much mirror area of the DMD as possible, we now have to measure small phase maps all over the DMD area and match them. According to our approach in Sec. 2.3, the matching of two small phase maps can be done by adding a linear gradient map to one of them. Since this linear gradient is calculated from the difference of the overlap of the two phase maps, an equal overlap between all neighbouring small phase maps is favourable. First, two small phase maps are matched. Then, we can match them together with a third small phase map, which again has an overlap. By continuously matching small phase maps with the precursory matched ones, we can retrieve

[10] Constantini phase unwrapping algorithm for Matlab by Bruno Luong
[11] 'loess' fit in Matlab with additional parameters 'Robust' and 'Bisquare'

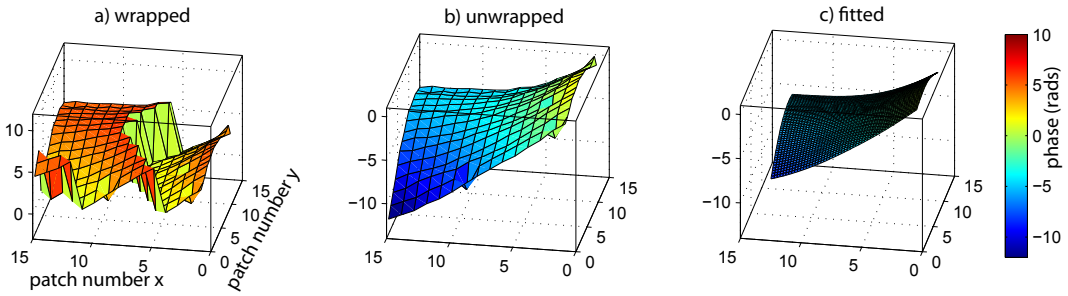

Figure 3.6: Phase map associated with a sampling region of 15x15 patches. a) shows the wrapped phase map we get directly from the fitting of the interference patterns. b) shows the unwrapped phase map and c) the final phase map, fitted with a locally weighted regression.

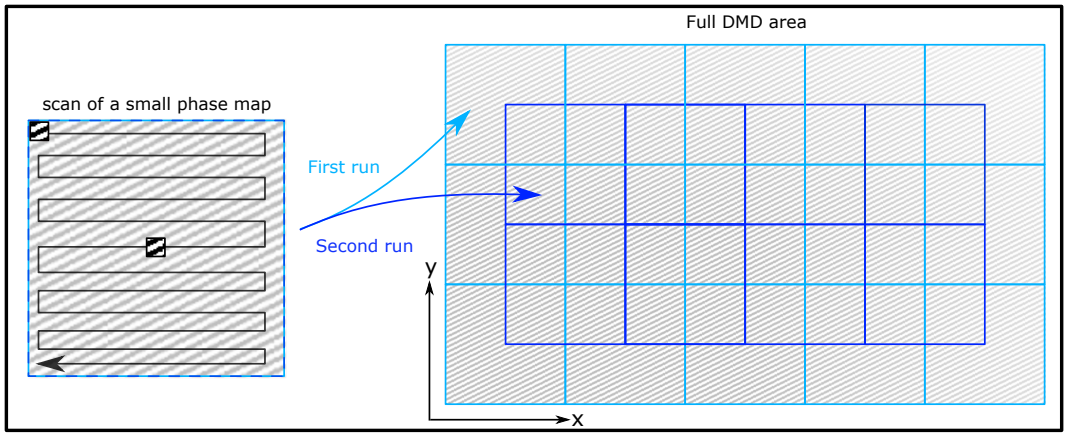

Figure 3.7: Retrieving the full phase map is done via measuring overlapping small phase maps across the DMD area. For the real setup for the first and second run 6x3 phase maps were recorded.

the full phase map for the DMD.

The measurement of all the small phase maps is done in two steps, see Fig. 3.7. First, we measure phase maps (bright blue) to cover the whole DMD area. Secondly, we take phase maps (dark blue) that are shifted by half its width in x and y. These small phase maps allow us now, to retrieve a full phase map for the whole DMD area.

To begin the matching procedure, we take two overlapping small phase maps on the border region of the DMD area, see Fig. 3.8. These first two neighbouring phase maps can be matched by taking the difference of their overlap, see Fig. 3.8 c). This difference is fitted with a two dimensional linear

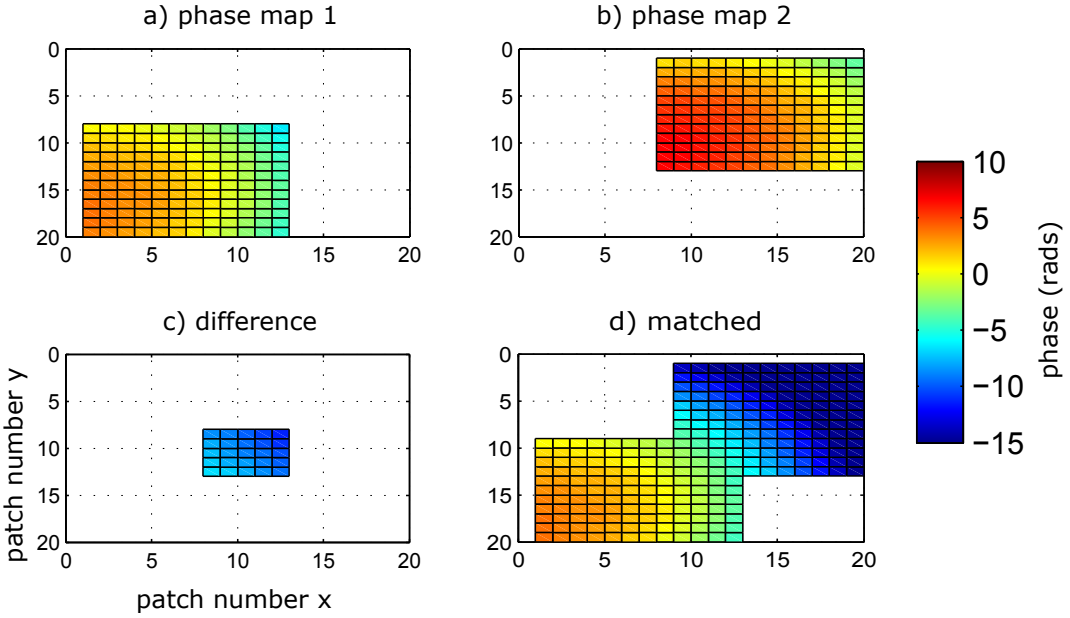

Figure 3.8: Matching procedure for two phase maps. First the difference of the overlap is calculated. This can be fitted with a linear gradient and an offset, which can the added to one of the maps to achieve a smooth transition between the two maps.

gradient map with an offset

$$\phi_{\text{match}}(x, y) = a + b_1 x + b_2 y. \tag{3.1}$$

Adding this gradient to one of the two phase maps results in a smooth transition between them, see Fig. 3.8 d). Next, we take these two matched phase maps and a third small phase map, that also overlaps with the already matched maps. Again the difference between the overlap gives a linear gradient, that can be added to the third map. This matches the third small phase map to the first two phase maps. To these three matched maps, a fourth one can be matched, and so on. This is done successively with each small phase map, until all maps are matched to one big phase map for the whole DMD. One important thing to notice is, that by adding gradients from small phase map to small phase map, an overall gradient is added to our final, big phase map. This leads to a shift of our used first order beam and therefore to a different beam path in the optical setup. To account for that, we add another linear gradient to the full phase map to flatten it back.

The complete phase map ϕ_{phase} for the DMD is shown in Fig. 3.9. It is difficult to distinguish aberrations, that are coming from the DMD itself and

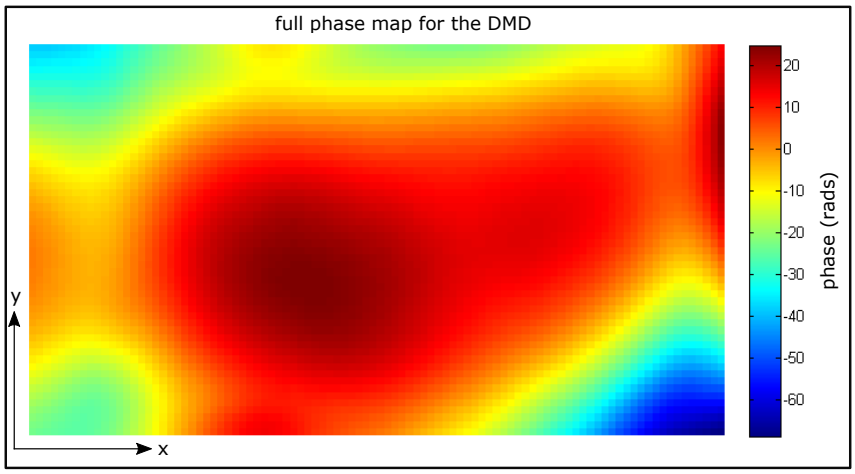

Figure 3.9: Complete phase map for the DMD. There are strong aberrations especially in the border region of the mirror area.

the ones coming from the lenses in the optical setup. While working with the DMD we noticed strong aberrations in the border region of the mirror area. This can be also seen in the final phase map in Fig. 3.9 where the correction has values between $+3 \cdot 2\pi$ and $-11 \cdot 2\pi$ at the border region.

Intensity map

The next step is to create the intensity map A_{int}, as described in Sec. 2.3. Patches of 60x60 mirrors are displayed. The value for the intensity can be measured simply by integrating the first order beam on the camera. We end up with an intensity map shown in Fig. 3.10. One can clearly see, that the beam is covering the full mirror area. At this point we have all necessary maps to start creating different beam shapes. The phase map will correct phase aberrations, present in the system and the intensity map accounts for the inhomogeneous incoming light intensity.

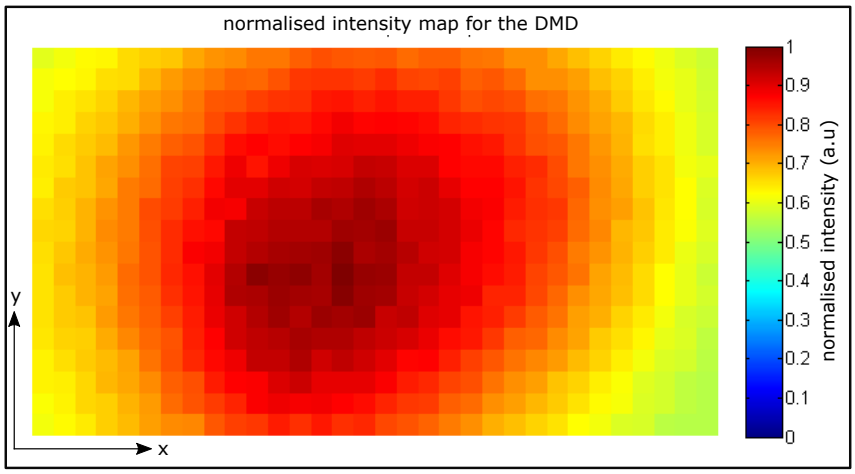

Figure 3.10: Intensity map for the setup. Scanned with a patch size of 60x60 mirrors.

3.3 Experimental results and created patterns

The two maps obtained in Sec. 3.2 can now be used to create different patterns. As explained in Sec. 2.3, besides the phase and intensity map, we also need a profile map, that contains the Fourier transformation of our desired beam shape. As a first example we will look at a simple Gaussian beam. Then we will move on to more complex shapes like higher order Hermite-Gaussian and Laguerre-Gaussian profiles.

Gaussian beam

As a first step, a normal Gaussian beam is created. To see the effect of the phase correction, we first apply only our intensity and profile map without the phase map on our grating, see Fig. 3.11 a). One clearly sees that the beam is completely deformed because of the aberrations present in the setup. However, when the phase map is applied, the aberrations are well compensated and we recover a nice Gaussian beam back, see Fig. 3.11 b).

Comparing Fig. 3.11 a) with b) one sees that the center of the beam pattern is shifted when applying the phase map. This comes from the fact, as discussed in Sec. 3.2, that still an overall gradient is present from the matching of the small phase maps. In principle one could also add another linear gradient to the phase map to shift the position of the corrected pattern completely back.

The corrected Gaussian beam is fitted with a two dimensional Gaussian

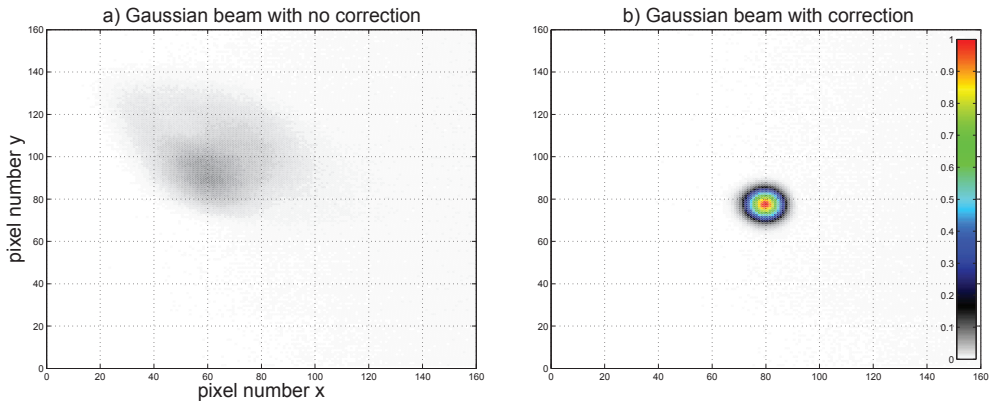

Figure 3.11: Gaussian beam displayed with the DMD. a) shows the displayed pattern without the phase map. Here all phase aberrations in the setup are present which washes the pattern out. In b) the phase map is applied. One clearly sees the correction of the aberrations in the appearance of a nice Gaussian beam shape.

fit. With an exclusion of values lower than 0.03 of the normalised maximum amplitude the fit yields a root-mean-square error of 1.13%[12]. In Fig. 3.12 a-d) a cut along two directions is shown. Especially a logarithmic plot reveals, that the pattern is Gaussian almost down to two orders of magnitude. At a value of $4{\cdot}10^{-3}$ an inhomogeneous background appears. Since this value is the lowest one, we can resolve with our 8 bit camera, it is not fully sure whether these single counts are real photons coming from background light or if they come from thermal excitations.

[12]The root-mean-square error is $\propto 1/\sqrt{N}$ with N being the number of fitted points. If all points from a camera picture are included in the fit, the background points would decrease the error, because less weight is putted on the actual pattern. Therefore a (arbitrary) cutoff of 0.03 was chosen and used for all other fits.

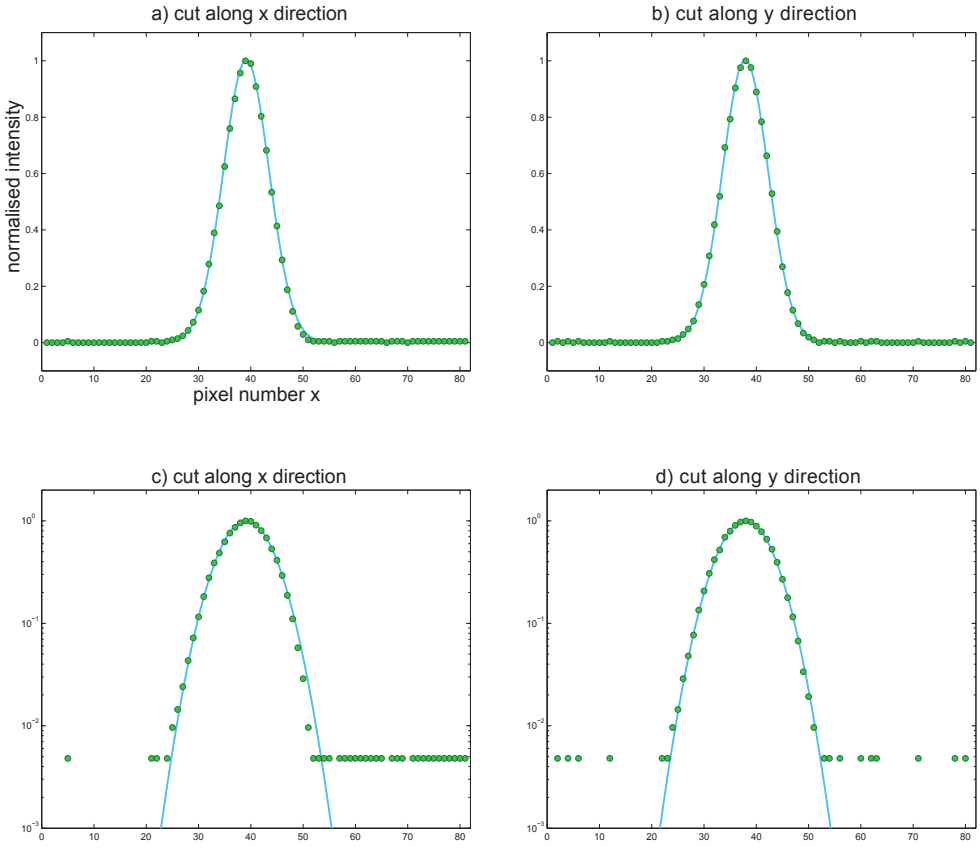

Figure 3.12: Cuts along two directions of the Gaussian beam, shown in Fig. 3.11. One sees that the pattern follows a Gaussian profile down to almost two orders of magnitude.

Hermite-Gaussian beams

One interesting set of patterns are $\mathrm{TEM_{nx,ny}}$ modes which appear for example in optical resonators. They can be described by a profile map

$$A_{\mathrm{profile,hermite}}(x,y) = \mathrm{H}_{nx}\left(\frac{\sqrt{2}x}{w}\right) \cdot \mathrm{H}_{ny}\left(\frac{\sqrt{2}y}{w}\right) \mathrm{e}^{-\frac{x^2+y^2}{w^2}} \tag{3.2}$$

where H_n is the one dimensional Hermite polynomial of order n. Here w defines the size of the pattern. Important to notice here is that the Hermite polynomials can be antisymmetric and hence can give negative values for the profile map. We cannot work with negative values, since we can only decrease the intensity coming from a certain DMD region. One nice way how these negative

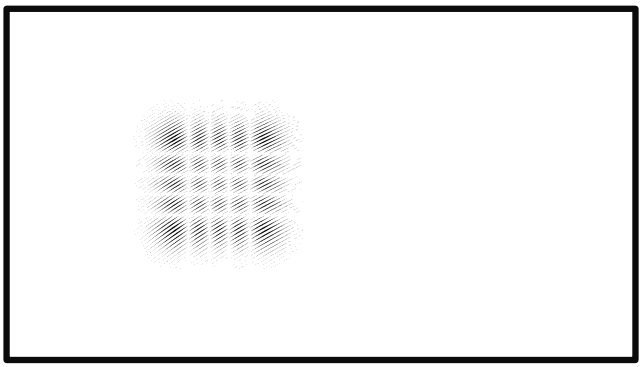

Figure 3.13: Complete grating for a Hermite-Gaussian mode. For comparison the full DMD area (black box) is drawn.

values can be treated is shown in Ref. [Zup13]. Here, simply a phase factor of $e^{i\pi} = -1$ is added in the regions for negative amplitudes. We can then use the absolute value of our profile map A_{profile} with this additional phase map $\phi_{\text{profile}}(x, y)$ to create the patterns.

To summarize: We have a phase map ϕ_{phase} and an intensity map A_{int}. We then create a profile map according to Eq. (3.2). From this profile map a new phase map for negative values ϕ_{profile} is calculated. Combining all of these maps, we end up with a grating shown in Fig. 3.13. Here, the size of the used grating compared to the full DMD area is illustrated. We will address a clearer insight into the possible pattern sizes and other limitations in Sec. 3.4.

In Fig. 3.14 we see a gallery of different camera pictures for $\text{TEM}_{\text{nx,ny}}$ modes that could be created with the DMD. The rms-errors of these pictures, taken from a two dimensional fit, range from 1.5 % for the (nx,ny) = (1,1) mode up to 3.6 % for (nx,ny) = (15,15). For the fits again points less than 0.03 of the maximum amplitude were excluded. To get a more quantitative view of the created patterns a cut through the (nx,ny)=(4,4) order and its two dimensional fit is shown in Fig. 3.14. When looking at the logarithmic scale, one sees that also here the patterns shape fits down to almost two orders of magnitude. On the linear plot, one sees that the peak amplitudes are varying slightly. This results from errors in our phase or amplitude map. As we have seen for the Gaussian beam, an imperfect correction for aberrations leads to a wrong intensity distribution and a blurring of our patterns. However, also errors in our intensity map could account for less amplitude in certain regions of our pattern.

By increasing the order (nx,ny) of our profile the structures on the grating get smaller and smaller. When these structures are as big as our grating period,

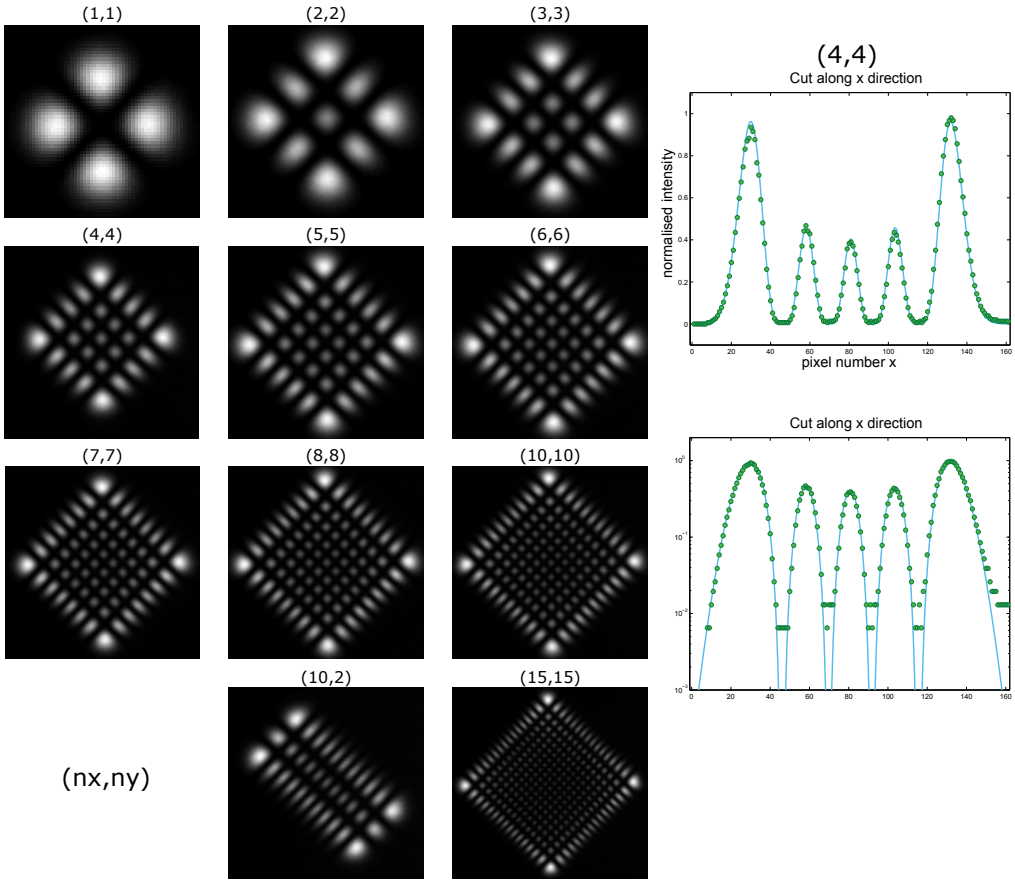

Figure 3.14: Different Hermite-Gaussian modes displayed with the DMD.

the grating cannot resolve them any more. Therefore it happens that each small peak in the grating pattern has a different number of mirrors available, which results again in different amplitudes in our beam pattern[13]. Therefore a bigger size for higher order grating patterns had to be chosen, which results in more sensitivity for phase map errors. This effect can be seen for (nx,ny)=(15,15), where the pattern shows already slight bending.

[13]Notice that on the camera we are looking at the Fourier transform of the grating pattern. Even though the Hermite-Gaussian modes are Fourier invariant, intensity coming from one peak on the grating pattern spreads over the full Fourier pattern. Therefore one small peak effects the full pattern on the camera.

Laguerre-Gaussian beams

Besides Hermite-Gaussian profiles we also prepare Laguerre-Gaussian profiles, described by

$$A_{\text{profile,laguerre}}(r) = r^{|l|} \mathrm{L}_p^l\left(2\frac{2r^2}{w^2}\right) \mathrm{e}^{il\phi} \mathrm{e}^{-\frac{r^2}{w^2}}. \tag{3.3}$$

Here $r = \sqrt{x^2+y^2}$ and $\phi = \text{atan2}(y,x)$ is the arcus tangent for all four quadrants. L_p^l is the generalised Laguerre polynomial with p radial nodes. The profile map has an inherent phase profile, coming from $\mathrm{e}^{il\phi}$. To all other phase maps that we have encountered so far, this is an additional one. It gives rise to a phase vortex of our beam in the Fourier plane, which leads to a vanishing intensity in the center for $l > 0$.

The different Laguerre-Gaussian modes are shown in Fig. 3.15. One nicely sees that the intensity is vanishing at the center, due to the phase vortex for $l > 0$. We created patterns up to $l = 2$. By increasing l more light is used from the outer DMD region of the pattern, which again results in more sensitivity for errors in our phase map. For $l = 0$ the main intensity is coming from the more central region of the pattern, where relative errors are less present, therefore the error for these modes are smaller. Especially when looking on the (l,p) = (3,2) mode one sees variances of the intensity across each ring.

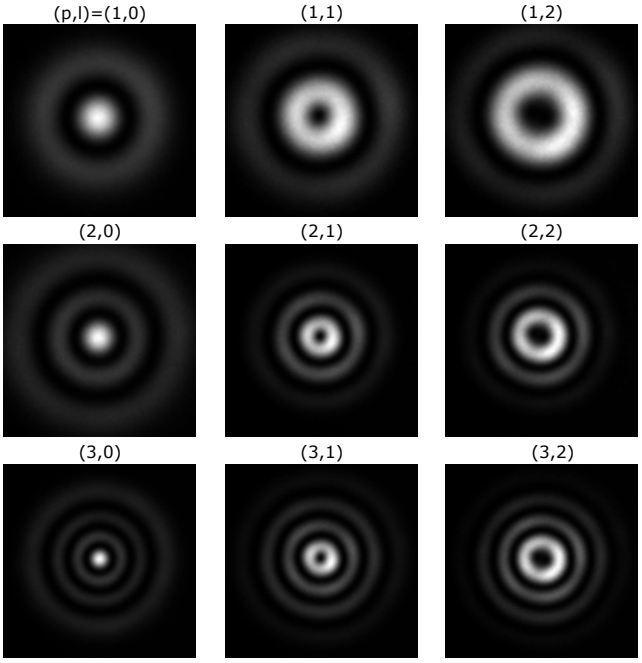

Figure 3.15: Laguerre-Gaussian beams displayed with the DMD.

3.4 Limitations and further improvements

So far we have seen possible beam profiles that can be created with the DMD. This section aims to discuss the limitations of the Fourier setup. I will go into more detail about the origin of different errors in the phase map. Then one important issue for the DMD is discussed, its power utilisation for the created patterns.

Phase map

Here I would like to give a clearer insight into the real sizes of our grating patterns, since this sets the number of pixels and therefore the degrees of freedom which we can use to create a beam profile. As mentioned already for the Hermite- and Laguerre-Gaussian beams, when increasing the size of our grating pattern problems from our phase map occurs. Therefore it is necessary to investigate this map further.

As a first test, the pattern was displayed on different regions of the DMD with the same size. In the central region of the mirror area the rms-error stayed nearly the same. Only for the border region, where strong aberrations are present, the beam shape gets worse, see Fig. 3.16. Here the rms-error raised

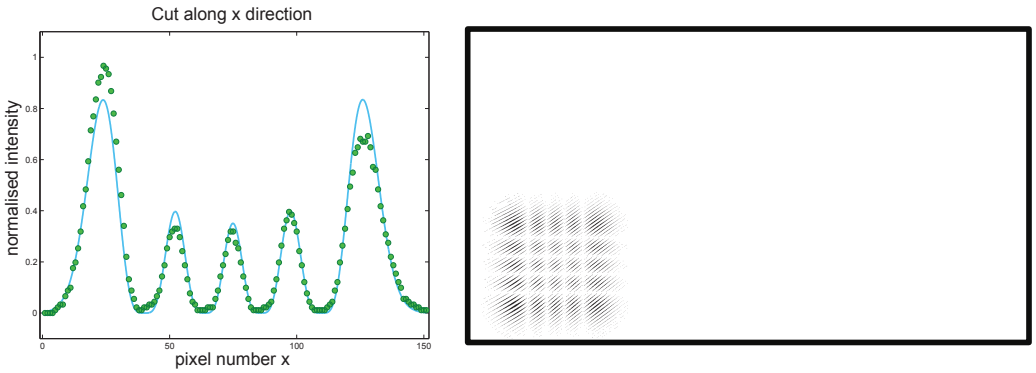

Figure 3.16: Displaying the pattern on the border region of the mirror area results in a worse beam shape. Here aberrations from the DMD area stronger and cannot be nicely compensated by the phase map.

up to 3.69 %. The aberrations here rapidly change the phase of our beam from 0 to 2π per roughly 50 pixels. Since this cannot be resolved with the used patch size, the phase unwrapping afterwards fails here. In principle a finer resolution could reduce this errors, but results in longer calculation time for the fitting procedure.

Since in the central region the phase errors do not depend on the position of the grating pattern. However, increasing the size of the patterns results again in a bigger rms error. Therefore, it becomes evident that the matching of the smaller phase maps introduces an error. Each time we add a linear gradient, which has a certain error, we introduce an error in the matched small phase map. These errors can now accumulate over more and more matched maps from a certain point. Therefore patterns, that use only neighbouring patterns show less error, because closer phase maps fit better together. If the pattern size is increased, further away phase maps are needed which have a bigger error relative to the central map. For the images shown in Sec. 3.3 only sizes of about 4x4 small phase maps are used. To improve this further, one should use a camera with a higher resolution, or use a pinhole with a photodiode as in Ref. [Zup13]. This would yield bigger single phase maps. Bigger phase maps would allow for more overlap between them and therefore less error of the linear gradient. Nevertheless, the used number of mirrors here, seems to be sufficient to create beam shapes, which fit to about 2 orders of magnitude.

Light utilisation

A very important issue concerning the DMD is its light utilisation. As mentioned already in Sec. 1.2 the beam shaping is done by simply switching certain mirrors to an OFF state. Thus inherently a lot of light power is simply dumped by the DMD. To get an estimate for the final power in our shaped beam profiles, we quickly recap the light utilisations at different steps. First losses occur because the DMD has a measured diffraction efficiency for our wavelength of about 75%. Secondly, the DMD constitutes a blazed grating (see Sec. 2.1). Even though the blaze condition is fulfilled, only about 92 % of the overall diffracted power could be sent into the $m = 6$ order. The rest is separated between the other orders. When displaying a plane grating all over the mirror area, already 50 % of our mirrors are switched OFF. Therefore only 50 % of the $m = 6$ orders light can be used after the DMD. The first order beam of our grating, which we use for beam shaping, carries only 10 % of this power since most of it is in the zero order. At this point it is clear, that our approach here is significantly limited in the utilisation of light. Up to here, only about 3.5% of the incoming light is really used for the first order of the uploaded grating.

Finally, to achieve different beam patterns the profile map has to be applied. Depending how different the shaped beam profile is compared to the incoming Gaussian beam, more or less mirrors need to be turned OFF to achieve the final pattern. Therefore it is clear, that maximally very few percent of the incoming laser light are really used for the modulated beam shape. Here not much can be improved. The only possibility is to shape the incoming beam to fit the displayed grating pattern as good as possible. For example if the profile map has a certain aspect ratio, the incoming beam should be made elliptical accordingly.

Chapter 4

Work in the lab: dipolar atoms in an optical lattice

During my master's thesis, I had the opportunity to work for about two months on the ERBIUM experiment in Innsbruck. First, we have exchanged the high temperature oven for the production of an erbium atomic beam. Then, I was involved in the first observation of the nearest-neighbour interaction of dipolar erbium atoms in a three-dimensional optical lattice.

At the beginning of this Chapter, I give a short overview of the current experiments in our group. Then I describe how laser beams can be used to create a three-dimensional optical lattice and describe the lattice setup in the experiment. Additionally, I will discuss the *Bose-Hubbard model* with an extension for magnetic, dipolar interactions. From here the nearest neighbour interaction can be understood. Finally, the measurement procedure and our results are presented.

4.1 The ERBIUM experiment

The experiment is a fully operating machine working with ultracold bosonic and fermionic erbium atoms. It can produce Bose-Einstein condesates (BECs) of bosonic ^{168}Er isotopes, containing up to 10^5 atoms, see Ref. [Aik12]. The ^{168}Er isotope can also be used to create Er_2 molecules via magneto-association with a Feshbach resonance [Fri15]. Also degenerate Fermi gases (DFG) can be created with the fermionic ^{167}Er isotope [Aik14].

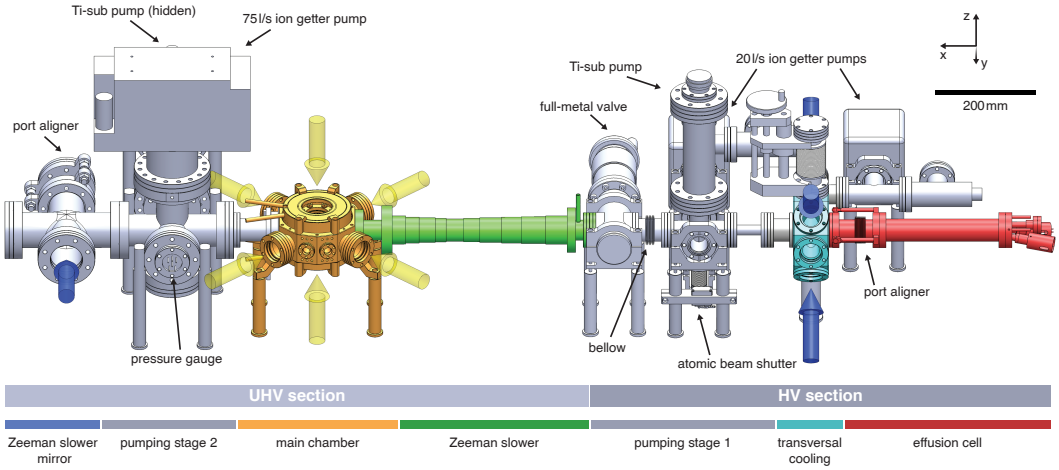

Figure 4.1: Chamber setup of the Erbium experiment. Picture taken from Ref. [Fri14]. With kind permission from Albert Frisch.

Overview of the apparatus

The machine and the working principles of the different components are fully described in Ref. [Fri14]. The apparatus includes the vacuum chamber and different laser systems for cooling light at 401 nm and 583 nm and trapping light at 532 nm, 1064 nm and 1570 nm.

The vacuum chamber is separated in two sections, which are connected with a differential pumping section. The first section contains a high temperature oven and a transversal cooling stage. The second section contains a Zeeman slower and the experimental chamber. Additionally both sections have pumping stages, to keep the needed vacuum level, see Fig. 4.1.

The high temperature oven uses an effusion cell, containing small pieces of solid erbium. It is typically operated at 1100°C. At this temperature erbium atoms can evaporate inside the oven. Additionally, a set of apertures is used to collimate the erbium beam emitted from the oven.

After the oven, a transversal laser cooling setup is used to transversally cool and optically collimate the atomic beam. This setup uses the broad 401 nm transition of erbium and increases the atom flux along the longitudinal direction. After the transversal cooling, the atoms enter a Zeeman slower. The Zeeman slower light is also operating at 401 nm. Its beam is counterpropagating with respect to the direction of the atomic beam and slows the atoms down in the longitudinal direction. Several coils create an inhomogeneous magnetic

field inside the Zeeman slower. This leads to a space-dependent Zeeman shift of the atomic resonances and compensates the Doppler shifts due to the reducing velocity of the atoms. With the Zeeman slower, atoms with a velocity smaller than 325 m/s can be slowed down to about 8 m/s.

At this point the atoms are slow enough to get captured by a narrow-line magneto-optical trap (MOT) [Fri12], operating at 583 nm. The corresponding transition of the erbium atoms has a linewidth of $\Gamma{=}2\pi{\cdot}190$ kHz and therefore a Doppler temperature $T_\mathrm{D} = \hbar\Gamma/(2k_\mathrm{B}) = 4.6\,\mu\mathrm{K}$. Here k_B is Boltzmanns constant. The MOT cools the atoms down to a temperature of 15 µK and additionally spin-polarises them, with an external bias field, to their lowest Zeeman sub-state.

To reach degeneracy the atoms are first loaded from the MOT into a horizontal 1064 nm optical dipole trap with a tunable geometry, see Ref. [Bai12]. For bosons an additional vertical 1064 nm laser beam is used to drive a forced evaporation of the atomic cloud. In the fermionic case, the atoms are loaded from the tunable 1064 nm trap into a crossed dipole trap similar to the bosonic case, but operated at 1570 nm. Again forced evaporative cooling is used to reach degeneracy.

For imaging, the atoms are released from the trap. After a time of flight of 27 ms an absorption image with a 401 nm laser pulse is created on a CCD camera.

Ultracold gases of erbium atoms

I will now briefly summarise two recent achievements of the ERBIUM team, achieved before I joined: the creation of the first erbium Bose-Einstein condensate and the first degenerate Fermi gas of erbium.

In 2012, the very first Bose-Einstein condensate (BEC) of ^{168}Er atoms could be produced, see Ref. [Aik12]. The atoms were first precooled in the narrow-line MOT and then loaded into the crossed optical dipole trap (ODT). The vertical beam of the ODT was operated at 1064 nm, whereas the horizontal beam at 1075 nm. The initial atomic cloud in the MOT had a temperature of 15 µK. The ODT was ramped up within 600 ms. After the ramping a total number of about 10^6 atoms with a temperature of 42 µK were loaded into the ODT. At this point the phase space density (p.s.d.) of the atomic cloud was four orders of magnitude below the critical p.s.d. of about 1, where Bose-Einstein condensation takes place. In a next step, forced evaporative cooling was performed by ramping down the trap intensities within 5.5 s. This allowed the hottest atoms to escape, while keeping the atomic sample thermalised. At a temperature of around 400 nK and an atom number of about 10^5, the onset

of Bose-Einstein condensation was seen in a bimodal peak, appearing on the absorption image of the thermal cloud. By evaporating even further, a pure BEC of $7 \cdot 10^4$ atoms with a non discernible thermal fraction was obtained. This erbium BEC provides the base for experiments conducted in the optical lattice as discussed in Sec. 4.3.

Later, in 2014, also fermionic ^{167}Er was brought to quantum degeneracy, see Ref. [Aik14]. The experimental procedure was very similar to the one used for the Bose-Einstein condensation. Again, the atoms were first precooled and spin polarised in the narrow-line MOT, leading to a gas of 10^7 atoms with a temperature of 7 µK. The atoms were first loaded from the MOT into a tunable, horizontal 1064 nm dipole trap and from that into a 1570 nm crossed ODT. Because of the Pauli exclusion principle, identical fermions do not scatter in s-waves at ultralow temperatures. This means that the atomic sample cannot thermalise and evaporative cooling will not work with s-wave collisions. A common work-around of this problem is to use fermions with different spin states, since they are not identical and hence can collide. However, for Erbium the situation is different, since even identical fermions exhibit a magnetic dipole-dipole interaction (DDI). Therefore, they can not collide in s-wave collisions, but via DDI. This feature was used to evaporatively cool identical fermions similar to the bosonic case. Finally, a degenerate Fermi gas (DFG) of $3{\cdot}10^4$ atoms could be achieved with a temperature as low as $0.11\,T_\mathrm{F}$. Here $T_\mathrm{F} = 1.06(5)\,\mu\mathrm{K}$ is the Fermi temperature of the system, see Ref. [Fri14].

4.2 The Bose-Hubbard model with dipolar, magnetic interactions

In this Section I will introduce the key ingredients to study the physics of ultracold erbium in a crystal made out of light. This includes an optical lattice, into which we later load the ultracold erbium atoms. Then, the magnetic dipole-dipole interaction, which is a main feature of erbium, is presented. Finally, the full *Bose-Hubbard Hamiltonian* of the system, will be discussed in more detail.

Optical lattice

A one-dimensional opical lattice is created using a retroreflected laser beam. The incoming and reflected beams interfere and create a periodic potential for the atoms. This potential resembles to a standing wave with a period of half the laser wavelength λ, see Fig. 4.2. By using retroreflecting beams in all three

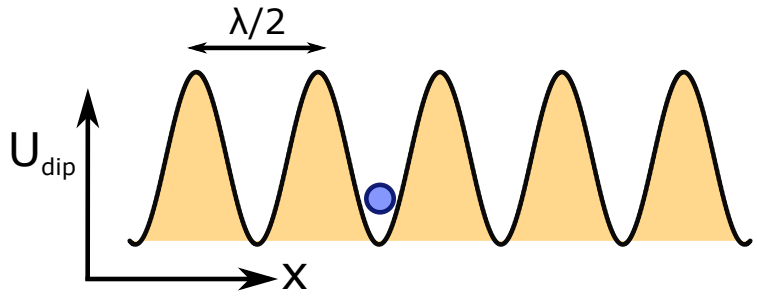

Figure 4.2: An atom in a standing wave potential, created by a retroreflected laser beam.

directions a three-dimensional optical lattice potential is formed. The different valleys define points in space, called lattice sites, on which the atoms can sit and tunnel in between.

The optical lattice potential can be described by

$$V(\mathbf{x}) = -V_x \mathrm{e}^{-2\frac{y^2+z^2}{w_x^2}} \sin^2(k_x x) - V_y \mathrm{e}^{-2\frac{x^2+z^2}{w_y^2}} \sin^2(k_y y) - V_z \mathrm{e}^{-2\frac{x^2+y^2}{w_z^2}} \sin^2(k_z z). \tag{4.1}$$

It can be seen as a superposition of one-dimensional standing waves with an amplitude V_i, a wave vector $k_i = 2\pi/\lambda_i$ and a Gaussian envelope. Since the atomic cloud is usually smaller than the used beam waists w_i, the Gaussian envelope of the potential can be approximated by

$$V(\mathbf{x}) \approx \underbrace{-V_x \sin^2(k_x x) - V_y \sin^2(k_y y) - V_z \sin^2(k_z z)}_{=V_\mathrm{lat}(\mathbf{x})} + \underbrace{\frac{m}{2}\left(\omega_x^2 x^2 + \omega_y^2 y^2 + \omega_z^2 z^2\right)}_{=V_\mathrm{ext}(\mathbf{x})}. \tag{4.2}$$

Here

$$\omega_x = \sqrt{\frac{4}{m}\left(\frac{V_y}{w_y^2} + \frac{V_z}{w_z^2}\right)}$$

is the resulting trapping frequency (cyclic permutated for y and z) of this harmonic approximation, see [Gre03]. From Eq. (4.2) we see, that the potential can be separated into two parts, a periodic three dimensional lattice and an additional harmonic confinement

$$V(\mathbf{x}) \approx V_\mathrm{lat}(\mathbf{x}) + V_\mathrm{ext}(\mathbf{x}).$$

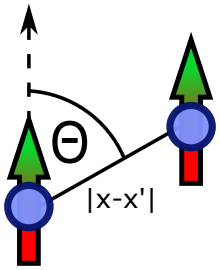

Figure 4.3: Schematic view of the magnetic dipole-dipole interaction between two parallel orientated atoms. The interaction sign and strength depend on the angle Θ and the distance $|\mathbf{x} - \mathbf{x}'|$ between the atoms.

Dipole-dipole interaction

Because of its large magnetic moment of $\mu = 7\,\mu_\mathrm{B}$ (μ_B is Bohr's magneton), erbium exhibits a sizable dipole-dipole interaction (DDI) in addition to the usual contact interaction. This DDI provides further aspects for ultracold lattice experiments and enriches the Hamiltonian of the system.

Since our atomic cloud is spin-polarised during the cooling in the MOT, all atomic dipoles are orientated in the same direction. Therefore the DDI potential between them is given by

$$U_\mathrm{DDI}(\mathbf{x}, \mathbf{x}') = \frac{\mu_0 \mu^2}{4\pi} \frac{1 - 3\cos^2\Theta}{|\mathbf{x} - \mathbf{x}'|^3}, \tag{4.3}$$

with μ_0 being the vacuum permeability. The potential is proportional to the square of the magnetic moment. Additionally it shows an angle dependence Θ, which is the angle between the interatomic axis and the direction of polarisation, see Fig. 4.3. The interaction strength falls of with the third power of the distance $|\mathbf{x} - \mathbf{x}'|$ between the atoms.

From Eq. (4.3) we see that the potential energy between the atoms vary continuously from attractive (Θ=0) to repulsive (Θ=90). In the following, we describe how the DDI enters into the Hamiltonian that describes our full system.

Extended Bose-Hubbard model

The Bose-Hubbard model is used to describe the behaviour of bosonic atoms, loaded into an optical lattice. So far, the majority of theoretical studies and all the experiments that studied Bose-Hubbard physics with ultracold atoms focussed on particles, interacting with short-range and isotropic (contact) interaction. For erbium, the DDI allows us to consider additional interaction

terms in the Bose-Hubbard Hamiltonian, that are usually neglected. We therefore speak of an *extended Bose-Hubbard model*, see Ref. [Dut15] for a thorough derivation.

To derive the Hamiltonian for our lattice system, we will start with its general form in second quantisation

$$\hat{H} = \int \mathrm{d}\mathbf{x}\hat{\psi}^\dagger(\mathbf{x})\Big[-\frac{\hbar^2}{2m}\Delta + V_{\mathrm{lat}}(\mathbf{x}) + V_{\mathrm{ext}}(\mathbf{x})\Big]\hat{\psi}(\mathbf{x}) + \\ + \frac{1}{2}\int\int \mathrm{d}\mathbf{x}\mathrm{d}\mathbf{x}'\hat{\psi}^\dagger(\mathbf{x})\hat{\psi}^\dagger(\mathbf{x}')\Big[\underbrace{\frac{4\pi\hbar^2 a_{\mathrm{s}}}{m}\delta(\mathbf{x}-\mathbf{x}')}_{\text{contact interaction}} + \underbrace{\frac{\mu_0\mu^2}{4\pi}\frac{1-3\cos^2\Theta}{|\mathbf{x}-\mathbf{x}'|^3}}_{\text{DDI}}\Big]\hat{\psi}(\mathbf{x}')\hat{\psi}(\mathbf{x}). \tag{4.4}$$

Here $\hat{\psi}(\mathbf{x})$ (resp. $\hat{\psi}^\dagger(\mathbf{x})$) describes the bosonic field operator, that destroys (creates) one particle at position $\mathbf{x}$. The first integral describes the single-particle part with its kinetic and potential energy coming from the lattice. The second part describes the atom-atom interaction, which consists of the contact interaction, proportional to the scattering length a_{s}, and the magetic dipole-dipole interaction. As shown in Ref. [Jak98], one can expand the bosonic field operators into a basis of Wannier-functions

$$\hat{\psi}(\mathbf{x}) = \sum_i \hat{b}_i \cdot w(\mathbf{x}-\mathbf{x}_i) \quad \text{and} \quad \hat{\psi}^\dagger(\mathbf{x}) = \sum_j \hat{b}_j^\dagger \cdot w^*(\mathbf{x}-\mathbf{x}_j). \tag{4.5}$$

The three-dimensional Wannier functions $w(\mathbf{x}-\mathbf{x}_i)$ are wave functions that are maximally localised on one single lattice site $\mathbf{x}_i$. They offer a possible wavefunction for an atom, that is well located on a single site, see Ref. [Dal05a]. The new operator $\hat{b}_i$ ($\hat{b}_j^\dagger$) is the bosonic annihilation (creation) operator, that destroys (creates) a particle on lattice site i (resp. j).

Inserting Eq. (4.5) into Eq. (4.4) we obtain integrals over Wannier functions on all possible lattice sites. Since these Wannier functions are well localised on their single lattice site, the overlap between two functions on different sites is in general small and most of the integrals can be neglected, see Appendix A.

The full Hamiltonian from Eq. (4.4) can be approximated in the following form

$$\hat{H} = -\sum_{\langle i,j\rangle} J\hat{b}_i^\dagger\hat{b}_j + \frac{1}{2}\Big(U_{\mathrm{c}} + U_{\mathrm{dd}}\Big)\sum_i \hat{n}_i(\hat{n}_i - 1) + \sum_i \epsilon_i\hat{b}_i^\dagger\hat{b}_i + \frac{1}{2}\sum_{\langle i,j\rangle} U_{\mathrm{NNI}}\,\hat{n}_i\hat{n}_j. \tag{4.6}$$

Here the first term desribes the *tunnelling rate* J for an atom on one lattice site to the next lattice site. The second term is called *on-site interaction* and is non-zero if more than one atom sits on the same lattice site. The on-site interaction

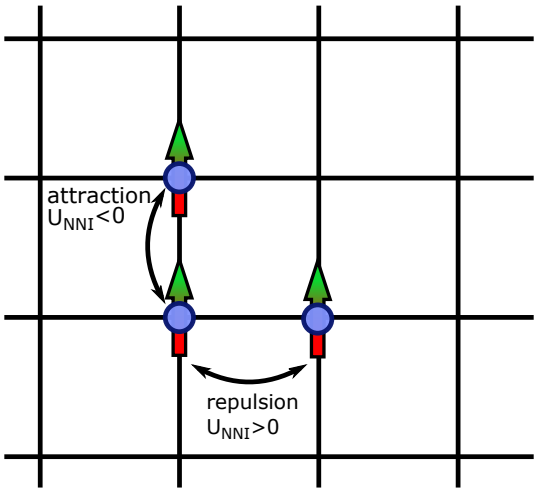

Figure 4.4: The nearest-neighbour interaction U_{NNI} depends on the orientation of the dipoles. For neighbouring lattice sites along the dipole orientation U_{NNI} is smaller than zero because the dipoles attract each other. For sites perpendicular to the dipoles U_{NNI} is bigger than zero.

has one contribution U_{c} from contact interaction (or s-wave scattering) between the atoms and one contribution U_{dd} from the magnetic DDI. The third term gives an energy offset ϵ_i due to the harmonic confinement of the lattice. This leads to smaller potential depths on lattice sites in the outer region of the lattice.

The last term in Eq. (4.6) is the magnetic DDI between neighbouring lattice sites $\langle i, j \rangle$. It is called the *nearest-neighbour interaction* (NNI) and is

$$U_{\mathrm{NNI}} = \frac{\mu_0 \mu^2}{4\pi} \int \int \mathrm{d}\mathbf{x}\mathrm{d}\mathbf{x}' |w(\mathbf{x} - \mathbf{x}_i)|^2 \frac{1 - 3\cos^2\Theta}{|\mathbf{x} - \mathbf{x}'|^3} |w(\mathbf{x}' - \mathbf{x}_j)|^2. \tag{4.7}$$

As can be seen in Eq. (4.7), the strength and the sign of the nearest neighbour interaction U_{NNI} depends on the orientation of the atomic dipoles. For neighbouring lattice sites along the orientation of the dipoles, the attraction between the atoms allows a lowering of their energy, thus $U_{\mathrm{NNI}} < 0$. In the other case, for lattice sites orientated perpendicular to the dipole orientation the energy of the atoms increase, because they repel each other, and $U_{\mathrm{NNI}} > 0$, see Fig. 4.4. For an atom at a specific lattice site, all neighbouring atoms contribute to its total energy and all U_{NNI} have to be summed up.

4.3 Measuring the nearest neighbour interaction with erbium in an optical lattice

Here, the experimental procedure for measuring the nearest-neighbour interaction is presented. First, the preparation of the system and the used optical lattice is discussed in more detail. Afterwards the measurement procedure and the final results are given.

Preparation of the lattice system

We first create a BEC of ^{168}Er atoms, as described in Sec. 4.1. The BEC typically contains $8 \cdot 10^4$ atoms and has a thermal fraction of about 20%. After the evaporation the lattice beams are adiabatically ramped up with a time constant of 150 ms to their final value. We use a wavelength of 532 nm (green) for our two horizontal lattice beams. Each lattice beam is created from a retro-reflected laser beam with 150 µm waist. The green light gives a distance of 266 nm between neighbouring lattice sites in the horizontal plane. In the vertical direction, we use a retro-reflected 1064 nm laser beam with a waist of 250 µm. This light results in a vertical lattice spacing of 532 nm, see Fig. 4.5.

The green 532 nm light is provided by a diode pumped laser[1]. We have about 1 W of green light available for each lattice beam. The 1064 nm light is delivered from a high-power, single-mode, ultra-narrow linewidth laser[2], that is also used for the horizontal dipole trap during the evaporation.

Usually the depth of the lattice potential is given in units of recoil energies $E_\mathrm{R} = \frac{\hbar^2 k_\mathrm{L}^2}{2m}$, which is for 532 nm (1064 nm) laser light $2\pi \cdot 4196$ Hz ($2\pi \cdot 1049$ Hz). Here m is the atomic mass, k_L is the lasers wave vector and $\hbar$ the reduced Planck constant.

With the available power for the different lattice beams, we can achieve lattice depths in the horizontal plane up to $30\,E_\mathrm{R}$. In the vertical direction we have possible lattice depths up to $200\,E_\mathrm{R}$. This range allows us to tune the tunnelling rate J along each lattice beam. For lattice depths of only a few recoil energies, tunnelling processes establish a phase correlation between the atoms on different lattice sites. This is know as the *superfluid phase*. For lattice depths bigger than about $14\,E_\mathrm{R}$, the tunnelling processes are suppressed and the atoms are pinned to specific lattice sites. This phase is the so called *Mott insulator* where no phase correlations between the atoms are present, see Ref. [Jak98, Gre03]. We therefore have the possibility to investigate the phase

[1] Verdi™ V-10 single frequency, diode-pumped laser with 10 Watt max. output from Coherent.

[2] Mephisto MOPA, 42 W, from Innolight (now Coherent)

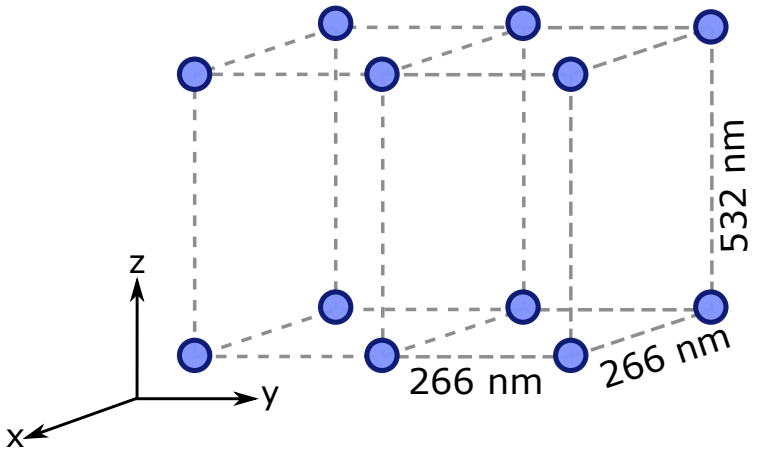

Figure 4.5: Lattice structure of the optical lattice. In the horizontal x-y-plane two 532 nm lattice beams create a lattice spacing of 266 nm. In the vertical z-direction a 1064 nm lattice beam creates a lattice spacing of 532 nm.

transition between these two phases with our erbium atoms.

As mentioned in Sec. 4.2 the dipolar character of erbium results in additional interaction terms in the Hamiltonian for our lattice system. In the following I will describe our measurements of the nearest-neighbour interaction U_{NNI}, which were carried out for the very first time.

Measurement procedure

Since our lattice spacing in the horizontal direction is 266 nm and 532 nm in the vertical direction, we have smaller spaced horizontal lattice sites and a bigger spacing in the vertical direction. Because the DDI falls off with $|\mathbf{x} - \mathbf{x}'|^3$ the interaction between atoms on different layers is much weaker than for atoms inside one layer. Therefore, we can restrict our following considerations to a two dimensional crystal of atoms.

After the MOT the dipoles are polarised along the vertical direction. The polarisation direction of the atomic dipoles can then be controlled with an external magnetic field. We rotate the dipoles adiabatically into the horizontal plane. For the following measurements, we orient them along one of the two horizontal lattice beams. After the rotation, the three-dimensional lattice is ramped up. The horizontal beams are ramped up to final lattice depths between 14 E_{R} and 20 $\mathrm{E_R}$. For the vertical 1064 nm beam we use lattice depths of 30 $\mathrm{E_R}$ and 40 $\mathrm{E_R}$. To look for systematic effects in our system, different combinations of these values are used to test the nearest neighbour interaction for different

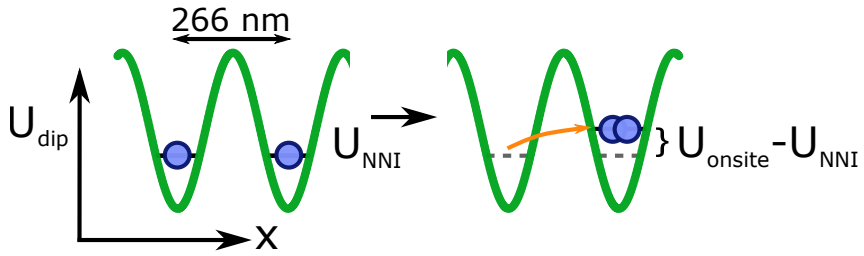

Figure 4.6: Schematic excitation process with parametric heating. Through intensity modulation of one lattice beam an atom can hop to the next lattice site, if the modulation frequency matches the energy condition.

lattice depths. It is important to notice that for these lattice depths we ensure that the atoms are always in a Mott insulating regime, where the tunnelling is suppressed and the atoms are pinned to a specific lattice site.

In a next step, we apply parametric heating via sinusoidally modulating the intensity of one of the two horizontal lattice beams, see Ref. [Köh05]. This modulation allows the atoms to hop to their next lattice site in the direction of the modulated laser beam. This is illustrated in Fig. 4.6. Here, we consider for simplicity a one dimensional double well with only two atoms. In the initial state each atom sits at one lattice site. In this case, the nearest neighbour interaction U_{NNI} is the only energy contribution we have to take into account, since here the tunneling rate J is negligible. Depending on the dipole orientation again $U_{\mathrm{NNI}} > 0$ or $U_{\mathrm{NNI}} < 0$, which corresponds to an energy shift compared to non magnetic atoms. After the hopping process, the two atoms sit on the same lattice site. The energy in this case is the on-site interaction U_{onsite} (contact and dipole-dipole), but we have lost the nearest neighbour interaction. The overall energy difference between this two configurations is therefore

$$\Delta U = U_{\mathrm{onsite}} - U_{\mathrm{NNI}}. \tag{4.8}$$

This energy can be calculated into a frequency $\Delta U/h$, with the Planck constant h, and is the frequency that needs to be provided for the atoms via the modulation frequency of the parametric heating. Meaning, if the modulation frequency is too small or too high, the atoms will not be able to hop, because the frequency does not match the hopping condition. Only if our modulation frequency hits the resonance at $\Delta U/h$ the hopping process will occur. This results in a depletion of the BEC, after ramping the lattice back down and taking a time-of-flight image. Therefore, by scanning the modulation frequency of the parametric heating, we get a depletion resonance in the BEC fraction. The center of this resonance is $\Delta U/h$.

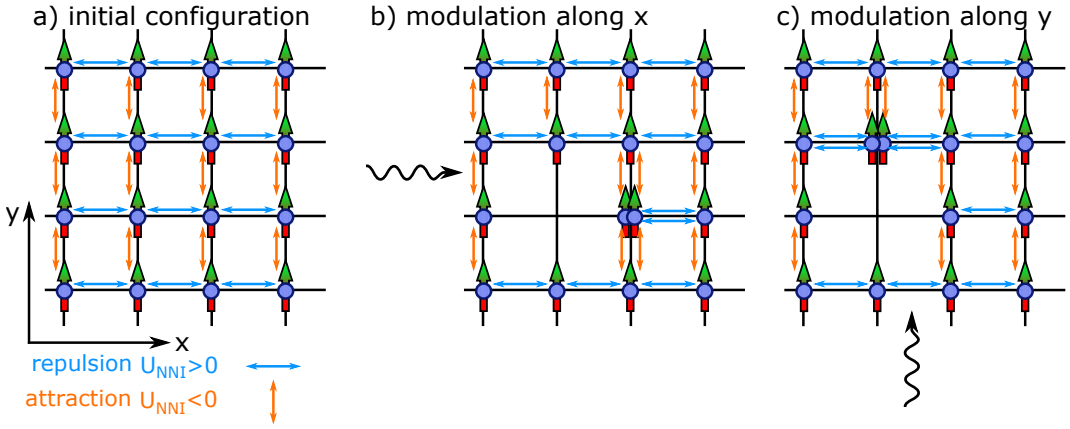

Figure 4.7: Procedure to measure the nearest-neighbour interaction. We start with a polarised sample in our optical lattice, where the dipoles are orientated along one of the horizontal lattice beams a). By modulating the intensity of one of the two horizontal lattice beams we allow the atoms to hop to a neighbouring site. Comparing hopping in different directions b) x and c) y allows us to extract the nearest neighbour interaction from the resonance frequencies. For more informations see text.

To see nearest-neighbour effects, we search for atom configurations that differ only by the nearest-neighbour interaction. In a simple model we look at 4x4 lattice sites, see Fig. 4.7. Here we assume that only one atom tunnels. If we apply parametric heating in x direction, the energy difference between the initial state and the final state is

$$\Delta U_{\text{mod x}} = U_{\text{onsite}} - U_{\text{NNI rep}}. \tag{4.9}$$

Again, we get the energy of the on-site interaction but loose one repulsive nearest-neighbour interaction. This can be seen by simply counting the arrows in Fig. 4.7.

If we perform the same measurement, but modulate along the y direction, the energy of the resonance becomes

$$\Delta U_{\text{mod y}} = U_{\text{onsite}} - U_{\text{NNI attr}}. \tag{4.10}$$

This time we again gain one on-site interaction but loose one attractive nearest-neighbour interaction (again, by counting the arrows).

By subtracting the resonance positions of the two measurements we end up with

$$\Delta U_{\text{mod y}} - \Delta U_{\text{mod x}} = U_{\text{NNI rep}} - U_{\text{NNI attr}} = \Delta U_{\text{NNI}}, \tag{4.11}$$

giving us the difference between the maximally repulsive and maximally attractive-nearest neighbour interaction. From Eq. (4.7) the theoretical value can be calculated and is for our system

$$\Delta U_{\mathrm{NNI\ theo}} = 89\,\mathrm{Hz}.$$

Final results

In our measurements we have measured ΔU_{NNI} for two dipole orientations, along x (first lattice beam) and along y (second lattice beam). This set of four measurements takes about 4 hours, leading to two data points.

Figure 4.8 shows two resonances for different modulation directions. Here the dipoles were aligned along the x direction. We scan the modulation frequency from 0 to 4.5 kHz for both lattice beams and fit the resonances with a Gaussian fit. We see a difference in the width of the resonance, depending on which beam we modulate. The width of the resonances varies between 0.8 and 1.1 kHz for all measurements. The shape of the resonances also appear slightly asymmetric, which is not fully understood up to now[3]. Compared to the width of the resonances, the shift due to nearest neighbour interaction is very small. In this specific case of Fig. 4.8 $\Delta U_{\mathrm{NNI}} = 72(30)$ Hz. When looking more carefully on Fig. 4.8, the points between 1.1 kHz and 1.5 kHz were neglected. Here a small resonance with half the resonance frequency of the main peak showed up. This small peak is simply due to higher harmonic excitations of our modulation.

We also look at the stability of the system via measuring the same configuration for a whole day. There we see a change of the left wing of the resonance. This leads effectively to a change of the fitted resonance position up to 100 Hz from measurement to measurement. We assume this comes from a change of our lattice system. Due to an unstable room temperature the lattice alignment can drift over time, which can lead to different loadings of the BEC into the lattice and also to different lattice depths between the runs. In order to overcome this drifts we take many data points for high enough statistics. Additionally the modulation along x and y is measured right after another.

Since the whole lattice had to be calibrated every day after the warm up, we usually had time for only one set of four measurements each day. In total we took 23 data points over several weeks. Each data point shows an error between ± 24 Hz and ± 51 Hz. The values for these errors are retrieved from the Gaussian fit of the resonances. A constant fit to all data points, weighted

[3] It could be due to an off-centered loading of the lattice resulting in an asymmetric broading of the resonance due to harmonic confinement.

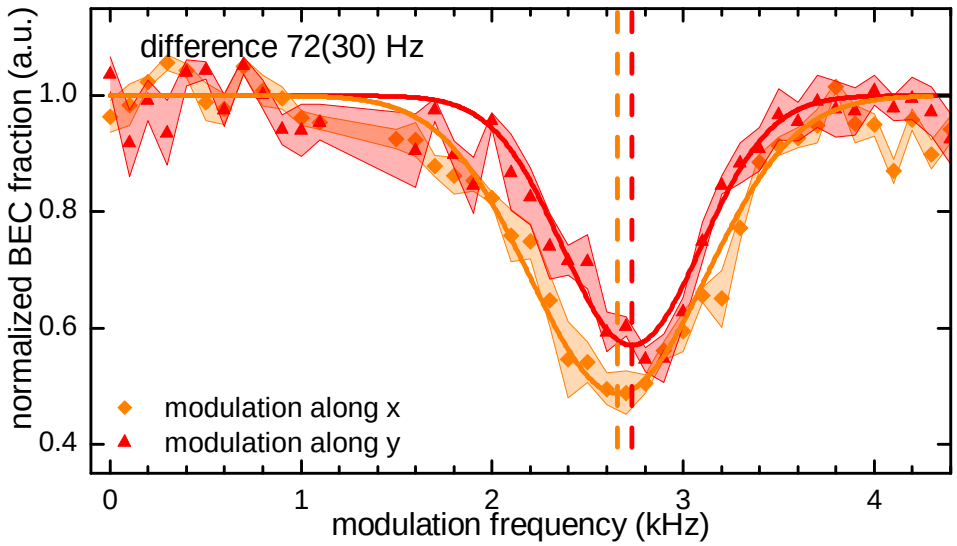

Figure 4.8: (color online) Frequency spectrum for two parametric heating measurements. The atomic dipoles are orientated along the x direction. We see a small shift of the resonance frequency between the modulation along x (squares) and y (triangles). This difference is due to nearest-neighbour interaction.

by the error bars yields a value of

$$\Delta U_{\mathrm{NNI\ exp}} = 81(8)\,\mathrm{Hz}$$

which agrees well with the theory.

Conclusion and Outlook

The goal of my master thesis was to produce spatially and temporally variable patterns of light using a digital micromirror device and study possible implementations in the ERBIUM experiment in Innsbruck.

After a literature study about spatial light modulators, it appear clear that light shaping could be realized with both, a liquid crystal SLM and a DMD. We opted for a DMD for its time stability. We created an optical setup using a Fourier configuration, in which the modulation takes place at the focus of the last lense. We choose this setup because it seems more easy to implement in our experiment.

The Fourier setup is used in combination with a displayed grating. The first order of this grating allows us to change the phase of the laser beam locally and therefore correct for phase aberrations, present in the optical setup. This can be done by simply shifting (or bending) the grating at specific regions on the DMD. To measure the phase aberrations two small patches of the grating can be displayed, where one is kept as a reference patch and the other one is scanned over a certain area of the DMD. The two patches create an interference pattern on a camera in the Fourier plane, from which the phase difference between the two patches can be calculated. The obtained small phase maps could then be matched together by adding a two dimensional linear gradient to the phase maps. With this technique the whole DMD area could be phase mapped. With the phase map we reached diffraction limited performance of the optical system. It was possible to recover a nicely Gaussian beam shape back from an uncorrected blurred spot, see Fig. 3.11 and Fig. 3.12. Additionally, when reducing the stripe widths of the grating locally, one can engineer different intensity distributions of the beam, which leads to different shapes in the Fourier plane. Here more complex beam shapes like Hermite-Gaussian and Laguerre-Gaussian beam shapes could be created, Fig. 3.14 and Fig. 3.15.

In a second part of my thesis work, I focussed on experiments in the ERBIUM lab and I was involved in the measurements of the nearest-neighbour interaction (NNI) of dipolar erbium atoms loaded into a three-dimensional optical lattice. There, I learned about lattice physics and the Bose-Hubbard

model with an extension for dipolar long-range interactions. To measure the NNI we excited the system along the two perpendicular directions of our horizontal lattice beams. The excitation was done by modulating the intensity of one lattice beam sinusoidally with a certain frequency. If this frequency hits the resonance condition, the atoms can hop to their neighbouring lattice site along the direction of the modulated beam. This hopping is associated with a loss of phase coherence between the atoms, which results in a worse recovery rate of the BEC when ramping down the lattice. Thus, from the resonance in the BEC fraction of the atomic cloud, we could extract the excitation frequency. For modulating along our first horizontal lattice beam, this frequency is the onsite interaction minus the attractive part of the NNI, see Chapter 4. When modulating with the second horizontal lattice beam, we again get the resonance frequency, consisting of the same onsite interaction minus the repulsive part of the NNI, see Fig. 4.8.

Finally, taking the difference between these two resonance frequencies results in a value for the nearest-neighbour interaction, which is expected to be 89 Hz for our system. To exclude systematic effects, we looked at different lattice depths and orientations of the erbium dipoles. Since our typical resonance widths lie between 0.8 kHz and 1.1 kHz, the difference due to the NNI is small. Additionally, we have also seen undirected drifts in our system during the day. For these two reasons we have taken 23 data points to get high enough statistics. Our final value of 81(8) Hz agrees well with the theory.

Momentum-resolved Bragg spectroscopy with a DMD

As an outlook, I would like to discuss one possible implementation of the DMD in ultracold atoms experiments - the *momentum-resolved Bragg spectroscopy* - which allows to measure the excitation spectrum of ultracold atomic clouds. The following give a short motivation for excitation spectras and emphasis their big variety depending on the experimental system.

Considering a non-interacting BEC in a homogeneous trap, the atoms show a simple excitation spectrum, that is the same as a classical, free particle

$$E(k)_{\text{non-int}} = \frac{p^2}{2m} = \frac{(\hbar k)^2}{2m}. \tag{4.12}$$

Here m is the atoms mass and $p = \hbar k$ its momentum, which can be associated with a wave vector k. If one takes weak interactions between the atoms into account, this spectrum changes, and can be well described within the so called *Bogolioubov theory*, see Ref. [And04]. Here the interactions between the atoms give rise to a change in the spectrum of elementary excitations [Ste02]

$$E(k)_{\text{weak-int}} = \sqrt{c^2(\hbar k)^2 + \left[\frac{(\hbar k)^2}{2m}\right]^2}, \tag{4.13}$$

where $c = \sqrt{gn/m}$ with $g = 4\pi\hbar^2 a_s/m$ being the contact interaction strength and n the constant density of the atomic cloud. For small k the first term dominates here and the excitation spectrum turns out to be linear in this regime. This linear regime is called *phonon-like*. In the region for big k, the first term in Eq. (4.13) can be neglected and the excitation spectrum becomes the *free-particle* excitation of Eq. (4.12).

Not only the interactions can modify the excitation spectrum, but also the trapping potential itself changes it. For example, if atoms are loaded into an optical lattice, the periodicity of the potential gives rise to a band structure spectrum, as in solids. As in solid state physics, the dispersion relation can be mapped into the first *Brillouin zone* in momentum space and exhibits bandgaps, see for example Ref. [Dal05a, Jak98]. When shaking a one dimensional optical lattice, the lowest lying band can exhibit even a *Roton-Maxon* feature, as has been experimentally observed in Ref. [Ha15].

Ultracold atoms in different optical traps show a big variety of their excitation spectras. In order to investigate these spectras an experimental tool is required, that allows to impart the energy E and the momentum k independently on the cloud. This can be achieved with momentum-resolved Bragg spectroscopy.

Bragg spectroscopy of a Bose-Einstein condensate was first demonstrated in Ref. [Ste99]. Here a BEC of Sodium atoms was created in a magnetic trap.

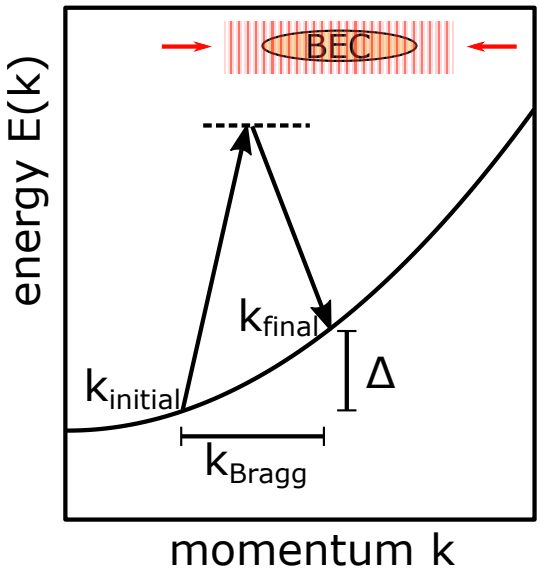

Figure 4.9: Momentum transfer of an atom in a Bragg process with two counterpropagating, detuned laser beams (red arrows). An atom with an initial momentum k_{initial} can absorb an atom of one laser beam and stimulatively emit a photon onto the other laser beam. This process results in a net momentum transfer k_{Bragg} that the atom picks up. However, the transfer only happens, if the energy provided by the frequency detuning Δ of the laser beams, matches the excitation energy to this specific momentum state.

Then two counter propagating, offresonant laser beams (Bragg pulses) were shone on the BEC, leading to a stand wave interference pattern with a wave vector k_{Bragg}, that is twice the lasers wave vector. A relative frequency detuning Δ between the two beams results in a movement of the interference pattern. The two beams allow now for a two photon process, if the detuning Δ matches the energy difference between the atoms initial and a final momentum state, see Fig. 4.9. An atom with an inital momentum k_{initial} can absorb a photon of one laser beam and stimulatively emit it into the other one. This results in a net momentum transfer $\hbar k_{\text{Bragg}}$ and the atom is brought to a higher momentum state k_{final}. When taking a time-of flight picture, these excited atoms will separate from the remaining cloud due to their higher momentum. Therefore one can find a resonance in the remaining atom number, when scanning the detuning Δ. In Ref. [Ste99] k_{Bragg} was not changed, therefore always the same momentum $\hbar k_{\text{Bragg}}$ was imparted on the atoms.

Later approaches like in Ref. [Ern10] implemented variable angles between the two Bragg pulses and could therefore create different k_{Bragg} values. Scan-

ning again the detuning for each value of k_{Bragg} allowed to extract the excitation energy. This was used to map out the band structure of ultracold atoms in an optical square lattice.

Recently, another approach for momentum-resolved Bragg spectroscopy was successfully demonstrated in Ref. [Ha15]. Here a digital micromirror device in combination with a high NA objective was used. They uploaded a grating pattern on the DMD and directly imaged it on the atoms. The resulting wave pattern at the position of the atoms could be moved around, by shifting the pattern on the DMD. Also the pattern's wave vector could be easily changed by changing the slit distances of the grating pattern on the DMD. This technique does not rely on frequency detunings Δ between two interfering beams. The energy for a Bragg process is here provided by the shifting speed v of the pattern via

$$E = pv = \hbar k_{\mathrm{Bragg}} v. \tag{4.14}$$

Here v was scanned to find the resonance position at which the atoms are again pumped into a higher momentum state.

On the following sites, I will give an additional approach to implement *momentum-resolved Bragg spectroscopy*. This approach will also use a DMD, but in combination with a Fourier setup. However, the setup was not implemented up to now in a real experiment. Therefore the following lines will just present a theoretical idea.

Momentum resolved Bragg spectroscopy with a DMD and a Fourier setup

The DMD offers us the possibility to display multiple Gaussian beams. These beams will overlap in the Fourier plane, where the camera or the ultracold atomic sample sits, and will form different interference patterns. By displaying three or four Gaussian beams, one can create lattice-like interference patterns, see Fig. 4.10. However, as we have seen in Sec. 3.4, the Fourier setup has a low power efficiency in the created beam profiles. Therefore these variable lattice patterns are not easily implemented to trap atoms, since the resulting potentials would be too shallow to keep the atoms.

If we now restrict us to the case of two displayed Gaussian beams, we get a standing wave interference pattern in the Fourier plane, see Fig. 4.11. We can now modify the wave vector and the direction of the interference pattern, by changing the distance between our two Gaussian patterns and rotate the full pattern on the DMD. This allows us to create wave vectors up to

$$k_{\mathrm{max}} = 2\mathrm{NA} \cdot k_{\mathrm{l}}, \tag{4.15}$$

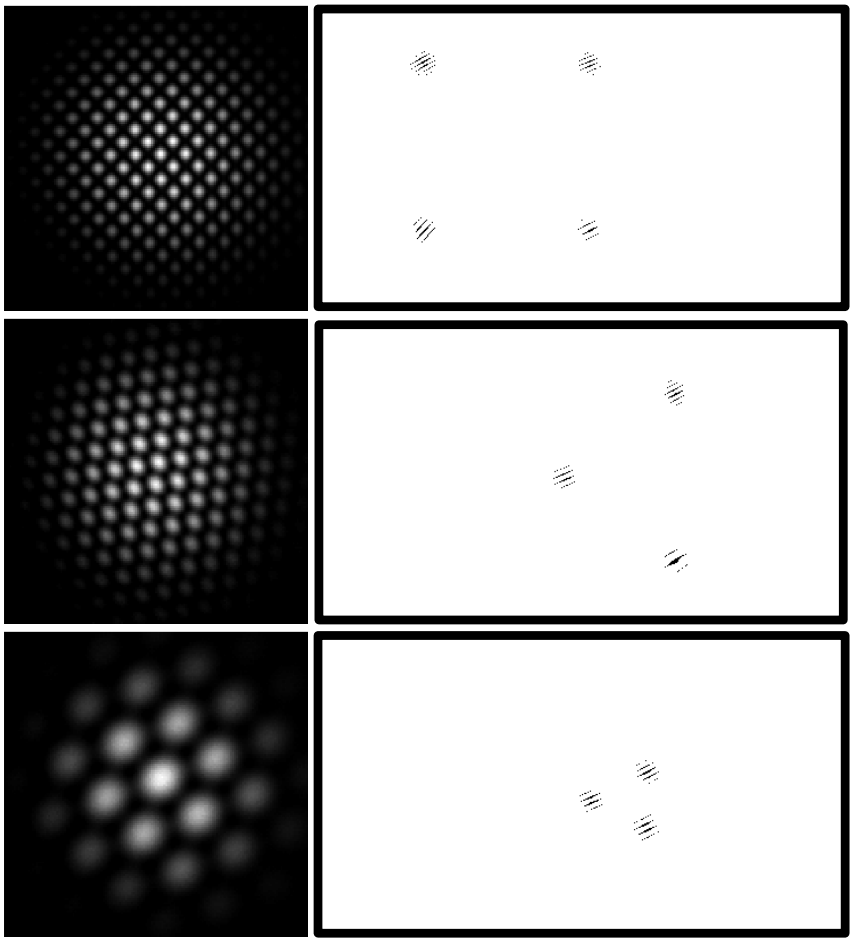

Figure 4.10: Via displaying multiple Gaussian beams, one can create lattice-like beam profiles in the Fourier plane. Images taken with a camera.

where k_l is the lasers wavelength and NA the numerical aperture of the lense. This means, that we can change k_Bragg from around zero to k_max continuously. One could also think about reflecting one of the two Gaussian beams out of the setup and direct it under a completely different angle on the atoms. This would be advantageous, if in the experiment, only a small NA can be achieved. Here one of the two beams could be shone on the atoms from a different view port. This would increase the possible wave vectors for the interference patterns even further.

The next question is, how to create a moving potential from this, so far static, interference pattern. As we have seen before, a moving potential can be created by introducing a frequency detuning between the two beams. At

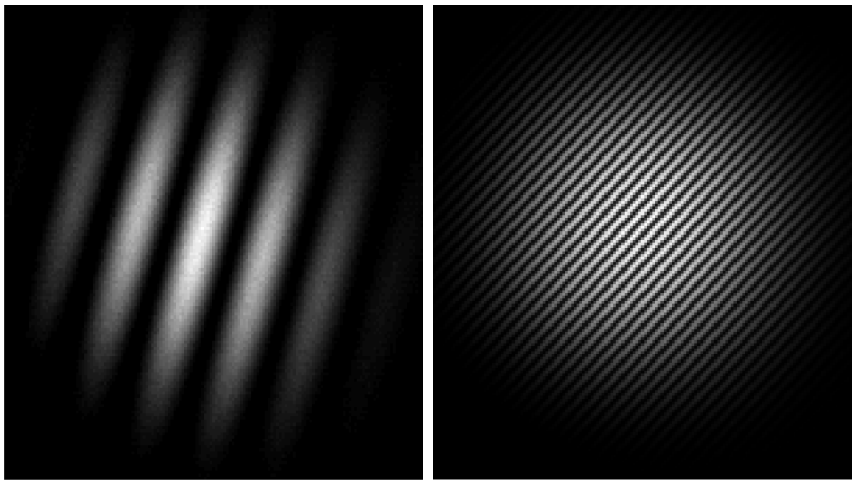

Figure 4.11: By displaying two Gaussian beams on the DMD, one gets an interference pattern that resembles a standing wave. Depending on the distance between the two patterns, one can engineer different wave vectors and angles for the interference pattern.

this point, we can simulate this frequency detuning by constantly shifting the phase

$$\phi(t) = v \cdot t$$

of one of the two beams. This means, that we shift the grating pattern of one of the two beams with a constant speed v. This gives rise to a frequency shift of the laser beam

$$\Delta\omega = \frac{d}{dt}(v \cdot t) = v.$$

Therefore, there is a frequency difference $\Delta\omega$ between the two beams, which causes the interference pattern to move. An example is given in Fig. 4.12, where the phase of one beam is shifted from 0 to 2π. One can clearly see, that the interference pattern moves along the white arrow (the red dot marks a point on the picture to make the movement more visible). How fast the interference pattern moves, depends on the frame rate, with which we shift our grating on the DMD. And how smooth it shifts depends on the resolution of our device. I Fig. 4.12, a grating constant of 15 pixels was used. Therefore one can shift the phase from 0 to 2π with a resolution of 15 steps. The additional pattern rate of 17.8 kHz for our DMD would therefore allow excitation frequencies of about 1 kHz. This is the maximum value needed in Ref. [Ha15], where the DMD was also used for Bragg spectroscopy.

At this point, we have everything at hand to perform Bragg spectroscopy.

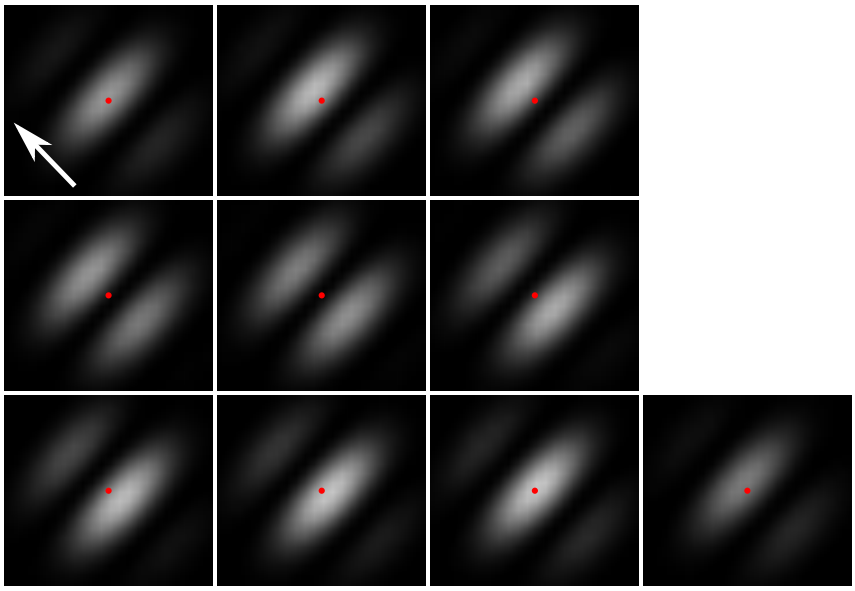

Figure 4.12: Shifting of the phase of one displayed Gaussian beam results in a shift of the interference pattern. The red dot marks the centre of the picture to see the shift more easily. The white arrow indicated the shifting direction.

We can change the momentum imparted on the atoms by changing the distance between the two Gaussian beam patterns on the DMD and therefore k_{Bragg}. And by shifting the grating of one of the two beams, we can introduce a frequency difference, to support energy for the atoms. Both can be individually varied.

Appendix A

Extended Bose-Hubbard Hamiltonian for dipolar interactions

For a more thoroughly description, the reader is referred to Ref. [Dut15]. To derive the Hamiltonian for a lattice system, one can start with its general form in second quantisation, as in Sec. 4.2,

$$\hat{H} = \int \mathrm{d}\mathbf{x}\hat{\psi}^\dagger(\mathbf{x})\Big[-\frac{\hbar^2}{2m}\Delta + V_{\mathrm{lat}}(\mathbf{x}) + V_{\mathrm{ext}}(\mathbf{x})\Big]\hat{\psi}(\mathbf{x}) + \\ + \frac{1}{2}\int\int \mathrm{d}\mathbf{x}\mathrm{d}\mathbf{x}'\hat{\psi}^\dagger(\mathbf{x})\hat{\psi}^\dagger(\mathbf{x}')\Big[\underbrace{\frac{4\pi\hbar^2 a_{\mathrm{s}}}{m}\delta(\mathbf{x}-\mathbf{x}')}_{\text{contact interaction}} + \underbrace{\frac{\mu_0\mu^2}{4\pi}\frac{1-3\cos^2\Theta}{|\mathbf{x}-\mathbf{x}'|^3}}_{\text{magnetic dipole int.}}\Big]\hat{\psi}(\mathbf{x}')\hat{\psi}(\mathbf{x}). \tag{A.1}$$

Again, $\hat{\psi}(\mathbf{x})$ ($\hat{\psi}^\dagger(\mathbf{x})$) describes the bosonic annihilation (creation) operator, that destroys (creates) one particle at position $\mathbf{x}$. The first integral describes the single particle part with its kinetic and potential energy coming from the lattice confinement. The second part describes the atom-atom interaction, which consists of the contact interaction and the magetic dipole interaction. As shown in [Jak98], one can expand the bosonic field operators into a basis of Wannier-functions

$$\hat{\psi}(\mathbf{x}) = \sum_i \hat{b}_i \cdot w(\mathbf{x}-\mathbf{x}_i) \quad \text{and} \quad \hat{\psi}^\dagger(\mathbf{x}) = \sum_j \hat{b}_j^\dagger \cdot w^*(\mathbf{x}-\mathbf{x}_j). \tag{A.2}$$

The three dimensional Wannier functions $w(\mathbf{x}-\mathbf{x}_i)$ are wave functions that are maximally localised on one single lattice site $\mathbf{x}_i$. They offer a possible

wavefunction for an atom, that is well located on a single site, see Ref. [Jak98, Dal05a]. The operator $\hat{b}_i$ ($\hat{b}_j^\dagger$) is the bosonic annihilation (creation) operator, that destroys (creates) a particle on lattice site i (j).

Inserting Eq. (A.2) into Eq. (A.1) we end up with integrals over Wannier functions on all possible lattice sites. Since these Wannier functions are well localised on their single lattice site, the overlap between two functions on different sites is in general small and most of the integrals can be dropped.

We first want to look at the first part of the Hamiltonian. The integrals over V_{ext} have a negligible contribution for Wannier functions on different lattice sites. We therefore neglect them here and only keep integrals over the same lattice sites

$$\hat{H}_{\text{ext}} = \sum_i \int \mathrm{d}\mathbf{x} V_{\text{ext}}(\mathbf{x}) |w(\mathbf{x}-\mathbf{x}_i)|^2 \hat{b}_i^\dagger \hat{b}_i \approx \sum_i V_{\text{ext}}(\mathbf{x}_i) \hat{b}_i^\dagger \hat{b}_i = \sum_i \epsilon_i \hat{b}_i^\dagger \hat{b}_i. \quad \text{(A.3)}$$

Usually in the literature $V_{\text{ext}}(\mathbf{x}_i)$ is written as ϵ_i, indicating the energy offset between different lattice sites due to the harmonic confinement.

The integrals over $-\frac{\hbar^2}{2m}\Delta + V_{\text{lat}}(\mathbf{x})$ give a constant energy offset for same lattice sites, which can be set to zero. To allow tunneling, also integrals over neighbouring lattice sites $\langle i,j \rangle$ are kept:

$$\begin{aligned} \hat{H}_{\text{tun}} &= -\sum_{\langle i,j \rangle} \int \mathrm{d}\mathbf{x} w^*(\mathbf{x}-\mathbf{x}_i) \Big[-\frac{\hbar^2}{2m}\Delta + V_{\text{lat}}(\mathbf{x}) \Big] w(\mathbf{x}-\mathbf{x}_j) \hat{b}_i^\dagger \hat{b}_j \\ &= -\sum_{\langle i,j \rangle} J_{i,j} \hat{b}_i^\dagger \hat{b}_j. \end{aligned} \quad \text{(A.4)}$$

Here $J_{i,j}$ is the tunnelling (or hopping) amplitude, which allows a particle to tunnel to the next lattice site. In general, it depends on the direction, in which the atom tunnels.

Regarding the second part of the Hamiltonian, the contact interaction term can also be restricted to Wannier functions on the same lattice site, which gives a *contact on-site interaction* U_{cont} for two atoms sitting on the same site

$$\begin{aligned} \hat{H}_{\text{cont.}} &= \frac{1}{2}\frac{4\pi\hbar^2 a_{\text{s}}}{m} \sum_i \int \mathrm{d}\mathbf{x} |w(\mathbf{x}-\mathbf{x}_i)|^4 \hat{b}_i^\dagger \hat{b}_i^\dagger \hat{b}_i \hat{b}_i \\ &= \frac{1}{2}\frac{4\pi\hbar^2 a_{\text{s}}}{m} \int \mathrm{d}\mathbf{x} |w(\mathbf{x})|^4 \sum_i \hat{b}_i^\dagger \left(\hat{b}_i \hat{b}_i^\dagger - 1 \right) \hat{b}_i \\ &= \frac{1}{2} U_{\text{cont}} \sum_i \hat{n}_i (\hat{n}_i - 1). \end{aligned} \quad \text{(A.5)}$$

Here we have used the bosonic commutation relations for the operators and that $\hat{b}_i^\dagger \hat{b}_i = \hat{n}_i$ is the number operator for the atom number on lattice site i.

New interesting terms, compared to the standard Bode-Hubbard model, appear due to the magnetic dipole-dipole interaction in the second part of the Hamiltonian. We get a contribution from Wannier functions on the same lattice site

$$\begin{aligned}\hat{H}_{\text{dd. onsite}} &= \frac{1}{2}\frac{\mu_0\mu^2}{4\pi}\sum_i \int\int \mathrm{d}\mathbf{x}\mathrm{d}\mathbf{x}'|w(\mathbf{x}-\mathbf{x}_i)|^2\frac{1-3\cos^2\Theta}{|\mathbf{x}-\mathbf{x}'|^3}w(\mathbf{x'}-\mathbf{x}_i)|^2\hat{b}_i^\dagger\hat{b}_i^\dagger\hat{b}_i\hat{b}_i \\ &= \frac{1}{2}U_{\text{dd}}\sum_i \hat{n}_i(\hat{n}_i-1) \end{aligned} \tag{A.6}$$

which has the same form as the contact on-site interaction. This *dipole-dipole on-site interaction* U_{dd} is due to the dipolar interaction between atoms on the same lattice site. In contrast to U_{cont} it has an angle dependence Θ. Here, for non-spherically-symmetric Wannier functions, the on-site interaction can be changed with the atomic dipole orientation Θ.

The last term, we want to consider here is the magnetic dipole-dipole interaction between neighbouring lattice sites. This is called the *nearest-neighbour interaction*

$$\begin{aligned}\hat{H}_{\text{NNI}} &= -\frac{1}{2}\frac{\mu_0\mu^2}{4\pi}\sum_{\langle i,j\rangle} \int\int \mathrm{d}\mathbf{x}\mathrm{d}\mathbf{x}'|w(\mathbf{x}-\mathbf{x}_i)|^2\frac{1-3\cos^2\Theta}{|\mathbf{x}-\mathbf{x}'|^3}w(\mathbf{x'}-\mathbf{x}_j)|^2\hat{b}_i^\dagger\hat{b}_i\hat{b}_j^\dagger\hat{b}_j \\ &= \frac{1}{2}\sum_{\langle i,j\rangle} U_{\text{NNI},i,j}\,\hat{n}_i\hat{n}_j. \end{aligned} \tag{A.7}$$

As can be seen in Eq. (A.7), the strength and the sign of the nearest-neighbour interaction $U_{\text{NNI},i,j}$ depends on the orientation of the atomic dipoles with respect to the lattice site i and j.

All this terms sum up to the extended Bose-Hubbard Hamiltonian

$$\hat{H} = -\sum_{\langle i,j\rangle} J_{i,j}\,\hat{b}_i^\dagger\hat{b}_j + \frac{1}{2}\Big(U_{\text{c}}+U_{\text{dd}}\Big)\sum_i \hat{n}_i(\hat{n}_i-1) + \sum_i \epsilon_i\hat{b}_i^\dagger\hat{b}_i + \frac{1}{2}\sum_{\langle i,j\rangle} U_{\text{NNI},i,j}\,\hat{n}_i\hat{n}_j. \tag{A.8}$$

Bibliography

[Abr10] M. Abramoff, M. Garvin, and M. Sonka, *Retinal Imaging and Image Analysis*, IEEE Reviews in Biomedical Engineering **3**, 169 (2010).

[Aik12] K. Aikawa, A. Frisch, M. Mark, S. Baier, A. Rietzler, R. Grimm, and F. Ferlaino, *Bose-Einstein Condensation of Erbium*, Phys. Rev. Lett. **108**, 210401 (2012).

[Aik14] K. Aikawa, A. Frisch, M. Mark, S. Baier, R. Grimm, and F. Ferlaino, *Reaching Fermi Degeneracy via Universal Dipolar Scattering*, Phys. Rev. Lett. **112**, 010404 (2014).

[And95] M. H. Anderson, J. R. Ensher, M. R. Matthews, C. E. Wieman, and E. A. Cornell, *Observation of Bose-Einstein Condensation in a Dilute Atomic Vapor*, Science **269**, 198 (1995).

[And04] J. O. Andersen, *Theory of the weakly interacting Bose gas*, Rev. Mod. Phys. **76**, 599 (2004).

[Bai12] S. Baier, *An optical dipole trap for Erbium with tunable geometry*, Master's thesis, LFU Innsbruck (2012).

[Bel11] D. Bellem, *Generation of Spatially and Temporally Varying Light Potentials in Optical Lattices*, Diploma thesis, LMU Muenchen and MPQ Munich (2011).

[Bil08] J. Billy, V. Josse, Z. Zuo, A. Bernard, B. Hambrecht, P. Lugan, D. Clément, L. Sanchez-Palencia, P. Bouyer, and A. Aspect, *Direct observation of Anderson localization of matter waves in a controlled disorder*, Nature **453**, 891 (2008).

[Blo14] B. J. Bloom, T. L. Nicholson, J. R. Williams, S. L. Campbell, M. Bishof, X. Zhang, W. Zhang, S. L. Bromley, and J. Ye, *An optical lattice clock with accuracy and stability at the 10^{-18} level*, Nature **506**, 71 (2014).

[Bos24] S. N. Bose, *Plancks Gesetz und Lichtquantenhypothese*, Zeitschrift f. Physik **26**, 178 (1924).

[Bou04] T. Bourdel, L. Khaykovich, J. Cubizolles, J. Zhang, F. Chevy, M. Teichmann, L. Tarruell, S. J. J. M. F. Kokkelmans, and C. Salomon, *Experimental Study of the BEC-BCS Crossover Region in Lithium 6*, Phys. Rev. Lett. **93**, 050401 (2004).

[Bra95] C. C. Bradley, C. A. Sackett, J. J. Tollett, and R. G. Hulet, *Evidence of Bose-Einstein Condensation in an Atomic Gas with Attractive Interactions*, Phys. Rev. Lett. **75**, 1687 (1995).

[Chi10] C. Chin, R. Grimm, P. Julienne, and E. Tiesinga, *Feshbach resonances in ultracold gases*, Rev. Mod. Phys. **82**, 1225 (2010).

[Col90] P. J. Collings, *Liquid Crystals*, Princeton University Press (1990).

[Dal05a] A. Daley, *Manipulation and Simulation of Cold Atoms in Optical Lattices*, Dissertation, LFU Innsbruck (2005).

[Dal05b] E. Dalimier and C. Dainty, *Comparative analysis of deformable mirrors for ocular adaptive optics*, Opt. Express **13**, no. 11, 4275 (2005).

[Dav95] K. B. Davis, M. O. Mewes, M. R. Andrews, N. J. van Druten, D. S. Durfee, D. M. Kurn, and W. Ketterle, *Bose-Einstein Condensation in a Gas of Sodium Atoms*, Phys. Rev. Lett. **75**, 3969 (1995).

[Day02] D. Dayton, J. Gonglewski, S. Restaino, J. Martin, J. Phillips, M. Hartman, P. Kervin, J. Snodgress, S. Browne, N. Heimann, M. Shilko, R. Pohle, B. Carrion, C. Smith, and D. Thiel, *Demonstration of new technology MEMS and liquid crystal adaptive optics on bright astronomical objects and satellites*, Opt. Express **10**, no. 25, 1508 (2002).

[Deg05] C. Degenhardt, H. Stoehr, C. Lisdat, G. Wilpers, H. Schnatz, B. Lipphardt, T. Nazarova, P.-E. Pottie, U. Sterr, J. Helmcke, and F. Riehle, *Calcium optical frequency standard with ultracold atoms: Approaching* 10^{-15} *relative uncertainty*, Phys. Rev. A **72**, 062111 (2005).

[Dei08] J. Deiglmayr, A. Grochola, M. Repp, K. Mörtlbauer, C. Glück, J. Lange, O. Dulieu, R. Wester, and M. Weidemüller, *Formation of Ultracold Polar Molecules in the Rovibrational Ground State*, Phys. Rev. Lett. **101**, 133004 (2008).

[Dut15] O. Dutta, M. Gajda, P. Hauke, M. Lewenstein, D.-S. Lühmann, B. A. Malomed, T. Sowiński, and J. Zakrzewski, *Non-standard Hubbard models in optical lattices: a review*, Rep. Prog. Phys **78**, 066001 (2015).

[Ein24] A. Einstein, *Quantentheorie des einatomigen idealen Gases*, Sitzungsberichte/Physikalische Klasse, Preussische Akademie der Wissenschaften **22**, 261 (1924).

[Ern10] P. T. Ernst, S. Götze, J. S. Krauser, K. Pyka, D.-S. Lühmann, D. Pfannkuche, and K. Sengstock, *Probing superfluids in optical lattices by momentum-resolved Bragg spectroscopy*, Nature Physics **6**, 56 (2010).

[Fri98] D. G. Fried, T. C. Killian, L. Willmann, D. Landhuis, S. C. Moss, D. Kleppner, and T. J. Greytak, *Bose-Einstein Condensation of Atomic Hydrogen*, Phys. Rev. Lett. **81**, 3811 (1998).

[Fri12] A. Frisch, K. Aikawa, M. Mark, A. Rietzler, J. Schindler, E. Zupanič, R. Grimm, and F. Ferlaino, *Narrow-line magneto-optical trap for erbium*, Phys. Rev. A **85**, 051401 (2012).

[Fri14] A. Frisch, *Dipolar Quantum Gases of Erbium*, Dissertation, LFU Innsbruck (2014).

[Fri15] A. Frisch, M. Mark, K. Aikawa, S. Baier, R. Grimm, A. Petrov, S. Kotochigova, G. Quéméner, M. Lepers, O. Dulieu, and F. Ferlaino, *Ultracold polar molecules composed of strongly magnetic atoms*, ArXiv e-prints 1504.04578 (2015).

[Fuk13] T. Fukuhara, A. Kantian, M. Endres, M. Cheneau, P. Schauß, S. Hild, D. Bellem, U. Schollwöck, T. Giamarchi, C. Gross, I. Bloch, and S. Kuhr, *Quantum dynamics of a mobile spin impurity*, Nature Physics **9**, 235 (2013).

[Gau13] A. L. Gaunt, T. F. Schmidutz, I. Gotlibovych, R. P. Smith, and Z. Hadzibabic, *Bose-Einstein Condensation of Atoms in a Uniform Potential*, Phys. Rev. Lett. **110**, 200406 (2013).

[Gre02] M. Greiner, O. Mandel, T. Esslinger, T. W. Hänsch, and I. Bloch, *Quantum phase transition from a superfluid to a Mott insulator in a gas of ultracold atoms*, Nature **415**, 39 (2002).

[Gre03] M. Greiner, *Ultracold quantum gases in three-dimensional optical lattice potentials*, Dissertation, LMU Muenchen (2003).

[Gri00] R. Grimm, M. Weidemueller, and Y. B. Ovchinnikov, *Optical Dipole Traps for Neutral Atoms*, Adv. In Atomic, Molecular, and Optical Physics **42**, 95 (2000).

[Gri05] A. Griesmaier, J. Werner, S. Hensler, J. Stuhler, and T. Pfau, *Bose-Einstein Condensation of Chromium*, Phys. Rev. Lett. **94**, 160401 (2005).

[Ha15] L.-C. Ha, L. W. Clark, C. V. Parker, B. M. Anderson, and C. Chin, *Roton-Maxon Excitation Spectrum of Bose Condensates in a Shaken Optical Lattice*, Phys. Rev. Lett. **114**, 055301 (2015).

[Hu04] L. Hu, L. Xuan, Y. Liu, Z. Cao, D. Li, and Q. Mu, *Phase-only liquid crystal spatial light modulator for wavefront correction with high precision*, Opt. Express **12**, no. 26, 6403 (2004).

[Jak98] D. Jaksch, C. Bruder, J. I. Cirac, C. W. Gardiner, and P. Zoller, *Cold Bosonic Atoms in Optical Lattices*, Phys. Rev. Lett. **81**, 3108 (1998).

[Joc03] S. Jochim, M. Bartenstein, A. Altmeyer, G. Hendl, S. Riedl, C. Chin, J. H. Denschlag, and R. Grimm, *Bose-Einstein Condensation of Molecules*, Science **302**, 2101 (2003).

[Joh60] B. Johnson, *Optics and optical instruments*, Dover Publications, Inc. (1960).

[Köh05] M. Köhl, H. Moritz, T. Stöferle, K. Günter, and T. Esslinger, *Fermionic Atoms in a Three Dimensional Optical Lattice: Observing Fermi Surfaces, Dynamics, and Interactions*, Phys. Rev. Lett. **94**, 080403 (2005).

[Kon88] N. Konforti, S.-T. Wu, and E. Marom, *Phase-only modulation with twisted nematic liquid-crystal spatial light modulators*, Opt. Lett. **13**, no. 3, 251 (1988).

[Kra09] S. Kraft, F. Vogt, O. Appel, F. Riehle, and U. Sterr, *Bose-Einstein Condensation of Alkaline Earth Atoms:* ^{40}Ca, Phys. Rev. Lett. **103**, 130401 (2009).

[Lu11] M. Lu, N. Q. Burdick, S. H. Youn, and B. L. Lev, *Strongly Dipolar Bose-Einstein Condensate of Dysprosium*, Phys. Rev. Lett. **107**, 190401 (2011).

[Mad00] K. W. Madison, F. Chevy, W. Wohlleben, and J. Dalibard, *Vortex Formation in a Stirred Bose-Einstein Condensate*, Phys. Rev. Lett. **84**, 806 (2000).

[Mod01] G. Modugno, G. Ferrari, G. Roati, R. J. Brecha, A. Simoni, and M. Inguscio, *Bose-Einstein Condensation of Potassium Atoms by Sympathetic Cooling*, Science **294**, 1320 (2001).

[Mu06] Q. Mu, Z. Cao, L. Hu, D. Li, and L. Xuan, *An adaptive optics imaging system based on a high-resolution liquid crystal on silicon device*, Opt. Express **14**, no. 18, 8013 (2006).

[Ni08] K.-K. Ni, S. Ospelkaus, M. H. G. de Miranda, A. Pe'er, B. Neyenhuis, J. J. Zirbel, S. Kotochigova, P. S. Julienne, D. S. Jin, , and J. Ye, *A High Phase-Space-Density Gas of Polar Molecules*, Science **322**, 231 (2008).

[Nog14] F. Nogrette, H. Labuhn, S. Ravets, D. Barredo, L. Béguin, A. Vernier, T. Lahaye, and A. Browaeys, *Single-Atom Trapping in Holographic 2D Arrays of Microtraps with Arbitrary Geometries*, Phys. Rev. X **4**, 021034 (2014).

[Pal05] C. Palmer, *Diffraction Grating Handbook*, Newport Corporation (2005).

[Pre15] P. M. Preiss, R. Ma, M. E. Tai, A. Lukin, M. Rispoli, P. Zupancic, Y. Lahini, R. Islam, and M. Greiner, *Strongly correlated quantum walks in optical lattices*, Science **347**, 1229 (2015).

[Rei88] F. Reinitzer, *Beiträge zur Kenntniss des Cholesterins*, Monatshefte für Chemie/Chemical Monthly **9**, no. 1, 421 (1888).

[Rob01] A. Robert, O. Sirjean, A. Browaeys, J. Poupard, S. Nowak, D. Boiron, C. I. Westbrook, and A. Aspect, *A Bose-Einstein Condensate of Metastable Atoms*, Science **292**, 461 (2001).

[Ste99] J. Stenger, S. Inouye, A. P. Chikkatur, D. M. Stamper-Kurn, D. E. Pritchard, and W. Ketterle, *Bragg Spectroscopy of a Bose-Einstein Condensate*, Phys. Rev. Lett. **82**, 4569 (1999).

[Ste02] J. Steinhauer, R. Ozeri, N. Katz, and N. Davidson, *Excitation Spectrum of a Bose-Einstein Condensate*, Phys. Rev. Lett. **88**, 120407 (2002).

[Ste09] S. Stellmer, M. K. Tey, B. Huang, R. Grimm, and F. Schreck, *Bose-Einstein Condensation of Strontium*, Phys. Rev. Lett. **103**, 200401 (2009).

[Tak03] Y. Takasu, K. Maki, K. Komori, T. Takano, K. Honda, M. Kumakura, T. Yabuzaki, and Y. Takahashi, *Spin-Singlet Bose-Einstein Condensation of Two-Electron Atoms*, Phys. Rev. Lett. **91**, 040404 (2003).

[Tak14] T. Takekoshi, L. Reichsöllner, A. Schindewolf, J. M. Hutson, C. R. Le Sueur, O. Dulieu, F. Ferlaino, R. Grimm, and H.-C. Nägerl, *Ultracold Dense Samples of Dipolar RbCs Molecules in the Rovibrational and Hyperfine Ground State*, Phys. Rev. Lett. **113**, 205301 (2014).

[TI13] Texas-Instruments, *DMD101: Introduction to Digital Micromirror Device (DMD) Technology* (2008, rev. 2013).

[Wan11] Z. Wang, L. Millet, M. Mir, H. Ding, S. Unarunotai, J. Rogers, M. U. Gillette, and G. Popescu, *Spatial light interference microscopy (SLIM)*, Opt. Express **19**, no. 2, 1016 (2011).

[Web02] T. Weber, J. Herbig, M. Mark, H.-C. Nägerl, and R. Grimm, *Bose-Einstein Condensation of Cesium*, Science **299**, 232 (2002).

[Wei00] A. M. Weiner, *Femtosecond pulse shaping using spatial light modulators*, Review of Scientific Instruments **71**, 1929 (2000).

[Zup13] P. Zupancic, *Dynamic Holography and Beamshaping using Digital Micromirror Devices*, Master's thesis, LMU Muenchen (2013).

Acknowledgment

First of all, I want to thank Francesca for giving me the possibility to work on this fascinating topic of spatial light modulation as a master thesis and for supporting me from the beginning on until now. I am also grateful that she gave me the chance to work on the ERBIUM experiment with the whole team, to get my first insights into scientific work. Besides the science, the whole team made it very easy for me, to decide for starting a Ph.D. here soon.

I want to thank Simon, for helping me from the beginning on in the lab up to now, where I am about to finish my thesis. Thank you, also for teaching me the main experiment. I enjoyed this time a lot.

Special thanks goes also to Albert, who left the team a few months ago. Thank you, for helping me especially with the setup of the DMD. I really appreciated your help in electronics, programming and also designing the casing. Also, thank you for your daily calls at midday for lunch. I wish you good luck in your new job and all the best for you and Sabine.

I am also thankful for Kiyotaka. Thank you, for always taking time for me and sharing your knowledge about optics. I wish you all the best for your new position in Japan.

Big thanks to Lauriane, who joined our team 3 months ago. I enjoyed our first weeks in the lab a lot. Also, thank you for correcting big parts of this thesis and for awaking my interests in bouldering.

I want to thank Manfred, for his time for me and for his great knowledge about electronics. Thank you, for always having an answer to everything.

To Tadas and Philipp: Thank you for your discussions about physics, travelling and all the rest. Also, thank you for being entertaining in our meetings and in our lunch breaks (in your particular traits).

I also want to thank all the people from Rudi's group and the people from Hanns-Christoph's group. It is very nice to work in such a professional and pleasant environment with a lot of exchange of knowledge.

Special thanks goes also to all the other master students around. I especially enjoyed the time with Dominic, Anton and Max.

Of course, none of the work, that we carried out would have been possi-

ble without the teams in the mechanical and the electronics workshop at the university. Thanks to all of you.

I want to thank my friends - Alex, Arzu, Adrian, Melanie, Flo, Hannes and Romina. For our game evenings, dinners and for the barbecues.

Thank you, Katharina and Niki, for being always there for me and for all your countless invitations to dinners and movie-nights.

I want to thank my parents, Doris and Hugo, for their support and love over the last 24 years. You always believe in me and made this life possible for me.

Finally, I want to thank Claudia. For loving me ♡.

Thank you!